

Rates of Stellar Tidal Disruption Events Around Intermediate-Mass Black Holes

JANET N. Y. CHANG,¹ LIXIN DAI,¹ HUGO PFISTER,¹ RUDRANI KAR CHOWDHURY,¹ AND PRIYAMVADA NATARAJAN^{2,3,4}

¹*Department of Physics, The University of Hong Kong, Pokfulam Road, Hong Kong*

²*Department of Astronomy, Yale University, New Haven, CT 06511, USA*

³*Department of Physics, Yale University, New Haven, CT 06520, USA*

⁴*Black Hole Initiative at Harvard University, 20 Garden St., Cambridge MA, 02138, USA*

ABSTRACT

Rates of stellar tidal disruption events (TDEs) around supermassive black holes (SMBHs) have been extensively calculated using the loss cone theory, while theoretical work on TDE rates around intermediate-mass black holes (IMBHs) has been lacking. In this work, we aim to accurately calculate the IMBH TDE rates based on their black hole masses and the stellar profiles of their host galaxies obtained from the latest observations. We find that IMBH TDEs from the center of small galaxies have an overall rate comparable to SMBH TDEs, while off-nuclei IMBH TDEs from globular clusters have a much lower rate. Very interestingly, we show that the rate of IMBH TDE per galaxy generally increases with the black hole mass, which is opposite to the trend seen in SMBH TDEs. Furthermore, we report that IMBH TDEs typically occur in the pinhole regime, which means that deeply plunging events are more likely for IMBH TDEs compared to SMBH TDEs. We also calculate the volumetric TDE rates for IMBH and SMBH TDEs and compare with observed rates.

1. INTRODUCTION

The study of intermediate-mass black holes (IMBHs) with masses that lie between stellar-mass black holes ($< 100M_{\odot}$) and supermassive black holes (SMBHs; $> 10^6M_{\odot}$), has sparked a lot of recent interest (see review by [Greene et al. 2020](#)). One important reason for studying IMBHs is that they provide insights into the formation and evolution of SMBHs through the cosmic history. In particular, different seeding scenarios of SMBHs, including gravitational runaway, death of population III stars, and direct collapse of gas clouds in the early universe ([Bond et al. 1984](#); [Portegies Zwart & McMillan 2002](#); [Bromm & Loeb 2003](#); [Portegies Zwart et al. 2004](#); [Lodato & Natarajan 2006](#)), lead to significantly different predictions for the IMBH number density; occupation fraction (the fraction of galaxies hosting black holes); and BH-galaxy scaling relations. Therefore, understanding the IMBH population is important as they serve as the bridge to the SMBH population. Additionally, in the Romulus and ASTRID cosmological simulations, in which central BHs are not forcefully pinned to the centers of their parent halos and host galaxies, a significant population of wandering IMBHs

are predicted in most, if not all, galaxies ([Ricarte et al. 2021b](#); [Di Matteo et al. 2023](#)). Therefore, observationally, we currently do not have a full census of the IMBH population.

Direct detection of IMBHs and measurements of their masses are rather challenging due to the limitations of current techniques. One of the most accurate methods is dynamical measurements, which are done via measuring the motions of stars or gases within the black hole's (BH) sphere of influence. However, this technique requires very high-resolution observations and therefore can only be applied to nearby galaxies, that are up to a few Mpc away ([Barth et al. 2009](#); [Neumayer & Walcher 2012](#); [den Brok et al. 2015](#); [Nguyen et al. 2017, 2019](#); [Kızıltan et al. 2017](#); [Lützgendorf et al. 2013, 2015](#); [Perera et al. 2017](#); [Baumgardt 2017](#); [Gerssen et al. 2002](#); [Noyola et al. 2010](#)). Another method for detecting and estimating IMBH masses is through their accretion luminosity. However, since accretion luminosity generally scales with the BH mass M_{BH} , with the low luminosities of IMBHs, it is difficult to discriminate the emission produced from accretion versus and young starbursts ([Cann et al. 2019](#)). As a result of these observational constraints, only a limited number (around 20-40) of IMBH candidates have been detected so far ([Greene et al. 2020](#)).

Recently, it has been proposed that tidal disruption events (TDEs) can provide a unique probe of IMBHs. TDEs are produced when a star ventures too close to a BH and gets ripped apart by extreme tidal forces (Rees 1988). Following the disruption, a large part of the stellar debris remains bound to the BH, and a luminous flare is produced through the collision or accretion of these debris. TDEs, it has been demonstrated, can help us constrain BH mass and spin (Kesden 2012; Leloudas et al. 2016; Mockler et al. 2019) and study BH accretion and outflow physics (Dai et al. 2021). Furthermore, since the disrupted stars are scattered into the “loss cone” through two-body interactions with other stars, the TDE rate can be used to probe the stellar population, dynamics and structure in the inner part of the host galaxy (Magorrian & Tremaine 1999; Wang & Merritt 2004).

Extensive theoretical calculations have been carried out of TDE rates. Magorrian & Tremaine (1999) and Wang & Merritt (2004) showed that assuming a simple isothermal stellar density profile and constant velocity dispersion, the typical TDE rates for SMBHs are around $10^{-4} - 10^{-3} \text{gal}^{-1} \text{yr}^{-1}$, with a weak dependence on the BH mass. Recently, more accurate studies of the TDE rates around SMBHs were conducted by Stone & Metzger (2016) and Pfister et al. (2020), who employed more realistic stellar profiles from observations of nearby, massive galaxies. The TDE rates from these galaxies can range between $10^{-8} - 10^{-3} \text{gal}^{-1} \text{yr}^{-1}$ and the large variation is introduced due to the differences in the host stellar structure. Furthermore, Pfister et al. (2020) found that the TDE rates in galaxies with nuclear star clusters (NSCs) can be enhanced up to 2 orders of magnitude. These NSCs are clusters of stars that reside in the center of galaxies, which are commonly found in galaxies with stellar masses less than $10^{10} M_{\odot}$ (Neumayer et al. 2020a). All of the works referenced above have focused on calculating the TDE rates in the SMBH regime, and they all find that the expected TDE rate from a galaxy on average declines with increasing mass of the SMBH or host galaxy.

Observationally, about 100 TDEs have been detected so far (Gezari 2021), a few of which are likely produced from IMBHs (Maksym et al. 2013; Wevers et al. 2017; Lin et al. 2018; Angus et al. 2022). IMBH TDEs are expected to generate different observational signatures compared to SMBH TDEs. Since the debris fallback time scales with $M_{\text{BH}}^{1/2}$ (Guillochon & Ramirez-Ruiz 2013), IMBH TDE flares have been suggested to have faster evolution timescales. For a solar type star TDE, the fallback timescale ranges between weeks to months for a SMBH but shortens to be only a few days for an

IMBH. Therefore, it has been proposed that fast blue optical transients (FBOTs) with rapid rise time could be powered by IMBH TDEs (Margutti et al. 2019; Kuin et al. 2019; Perley et al. 2019). On the other hand, stellar debris can circularize very slowly around IMBHs since the stream self-collisions are weak (Dai et al. 2015; Shiokawa et al. 2015; Wong et al. 2022), which can possibly greatly lengthen the TDE flare rise timescale. More theoretical modellings are needed to check which effect dominates and whether TDE flares do evolve more fastly around IMBHs than SMBHs. In addition, IMBH TDEs would be dimmer than SMBH TDEs if their accretion power is Eddington-limited, although recent numerical studies suggest that super-Eddington accretion can also be radiatively efficient for optimal conditions (Jiang et al. 2014; McKinney et al. 2015). Furthermore, IMBHs may not only be harbored in centers of small galaxies but may also be hosted in globular clusters. It has also been shown that during galaxy mergers the satellite galaxies which potentially host IMBHs take a long time to merge with the central SMBH (Pfister et al. 2021). Therefore, some fraction of IMBH TDEs are likely to be found off-center in massive galaxies. Last but not least, IMBHs can disrupt compact stars such as white dwarfs (WDs) (MacLeod et al. 2016; Law-Smith et al. 2017), which also produces gravitational waves and promotes the prospect of conducting multi-messenger studies of TDEs (Eracleous et al. 2019).

While it has been speculated that a large fraction of the TDEs can be produced from IMBHs, the TDE rate calculation in this regime has been severely lacking. Only very recently, Polkas et al. (2023) calculated the time-dependent rate of TDEs including the contribution from IMBH population from centers of galaxies, by analyzing the results from a semi-analytical galaxy formation and evolution model. They report that as M_{BH} increases, TDE rate first increases until $M_{\text{BH}} \sim 10^{5.5}$ and then flattens before turning over to decrease with M_{BH} at higher masses. However, in their model, the NSC component, which impacts the TDE rates significantly, was implemented based on a simple phenomenological model. On the other hand, for IMBHs in globular clusters (GCs), Ramirez-Ruiz & Rosswog (2009) estimated their TDE volumetric rates to be around $4 \times 10^{-6} \text{yr}^{-1} \text{Mpc}^{-3}$. Recently, Tang et al. (2024) further estimated that the TDE rate from a individual GC lies between 10^{-8}yr^{-1} to 10^{-5}yr^{-1} with a dependence on the GC stellar mass.

We aim to fill the gaps in these estimates by calculating the IMBH TDE rate from a different perspective. In this work, we combine the loss cone dynamics calculations adopting more realistic stellar profiles for galax-

ies and stellar clusters hosting IMBHs, with the latter obtained from recent state-of-the-art observations. We note that these IMBH-hosting galaxies and clusters can only be resolved at very low redshifts. After calculating the TDE rates from individual IMBHs, we apply the black hole mass function and occupation fraction, also obtained from observations, to calculate the volumetric IMBH TDE rates.

Our paper is structured as follows. We provide a description of the methodology in Section 2, where we introduce the observed samples of IMBH hosting galaxies and stellar clusters as well as the loss cone dynamics calculation. We report the results of the computed theoretical IMBH TDE rates and compare them to SMBH TDE rates in Section 3.1, and calculate the contribution from the pinhole regime and the diffusive regime to the rates in Section 3.2. We analyze the dependence of TDE rates and pinhole fraction on the stellar profile in Section 3.3. Next, we calculate the volumetric IMBH and SMBH TDE rates and compare them to observed rates in Section 3.4. The distribution of the penetration parameter β in IMBH and SMBH TDEs is computed and presented in Section 3.5. We then investigate the turnover behaviors of the rates in Section 3.6. Lastly, we close by with a summary and discussion of our results in Section 4.

2. METHODOLOGY

2.1. IMBH sample

We collate a sample of 23 observed IMBHs for our TDE rate calculation. These IMBHs are all nearby with dynamically measured masses. This ensures that the stellar profiles close to the IMBHs are also well constrained, which permits accurate TDE rate calculations.

For constructing this IMBH sample, we start from the IMBHs listed in Table 2-4 in Greene et al. (2020) and only select those with dynamical BH mass measurements. We also add the two most recently observed TDEs, B023-G78 (Pechetti et al. 2022) and AT2020neh (Angus et al. 2022). The latter is argued to be an IMBH TDE, which however does not have its BH mass measured dynamically. However, since its host galaxy profile is available in the published literature, we include it in our sample.

Amongst these 23 IMBHs, 15 reside in the centers of their host galaxies (hereby referred to as IMBH-galactic nucleus, or IMBH-GN), that are listed in Table A.1. The other 8 IMBH candidates reside in globular clusters which are off-nuclear (and are referred to as IMBH-off nucleus, or IMBH-ON hereafter), and these are listed in Table A.2.

The BH mass is a parameter which impacts the TDE rate and demographics calculation. Several IMBH-GNs in our list from Neumayer & Walcher (2012) are reported with both a best mass estimate ($M_{\text{BH,best}}$) and a maximum mass constraint ($M_{\text{BH,max}}$), while the others only have a single mass estimate. For IMBH-ONs, their mass measurements are less accurate, and sometimes for the same IMBH the $M_{\text{BH,best}}$ measurement from one published source differ from and be larger than the $M_{\text{BH,max}}$ constraint from another reported measurement. Here, we adopt the largest value of the reported M_{BH} s for IMBH-ONs and consider them all as $M_{\text{BH,max}}$. We then further split the sample on the basis of the quality of the measurements - IMBHs with $M_{\text{BH,best}}$ measurements, and those with tentative measurements - IMBHs with $M_{\text{BH,max}}$ constraints only. As an exception, the IMBH-GNs from Neumayer & Walcher (2012), have $M_{\text{BH,best}}$ but we consider them as tentative measurements, since their calculation is based on a single integrated velocity dispersion which is dominated by the stellar mass in large radii (Neumayer et al. 2020b). Tentative measurements are given a 50% weight when obtaining several fits in later sections. There is also one special case of NGC 4395, for which the IMBH mass has been measured using both dynamical measurements (e.g., den Brok et al. 2015) and reverberation (Woo et al. 2019; Cho et al. 2021) techniques and the two M_{BH} values have an order-of-magnitude discrepancy. For this IMBH, we take the geometric mean of these two M_{BH} values for the TDE rate calculation.

2.2. Stellar profiles of the galaxies and clusters hosting IMBHs

The stellar profiles of the galaxies or clusters hosting the IMBHs in our sample have all been previously modeled using either the Sersic profile (Barth et al. 2009; Neumayer & Walcher 2012; den Brok et al. 2015; Kızıltan et al. 2017; Nguyen et al. 2019; Davis et al. 2020; Angus et al. 2022) or the King profile (Gerssen et al. 2002; Noyola et al. 2010; Lützgendorf et al. 2013, 2015; Baumgardt 2017; Perera et al. 2017; Pechetti et al. 2022). For the galaxies hosting IMBH-GNs, we adopt their stellar profiles fitted to Sersic models, which is described further in Section 2.2.1. However, the stellar profiles of the clusters hosting IMBH-ONs have only been fitted using the King model in the literature, and this in turn is described in Section 2.2.2. We list the fitted parameters for the IMBH-GC and IMBH-ON sources in the collated sample in Table A.1 and Table A.2 respectively.

Low-mass galaxies are often observed to host NSCs (Neumayer et al. 2020a). Therefore, one can see that some galaxies in Table A.1 can have more than one

component describing their stellar profile. Moreover, we note that the 8 galaxies from [Neumayer & Walcher \(2012\)](#) have measurements of the stellar profiles of only their NSCs but not of their bulges. This, however, does not affect our TDE rate calculation, since NSCs are significantly denser than bulges and therefore are expected to dominate the TDE rates ([Pfister et al. 2020](#)). Similarly, B023-G78 was also modeled with an inner King profile and an outer Sersic profile. For the same reason, we have only considered the fitted inner King profile for the TDE rate calculations.

2.2.1. Sersic profile fits to TDE hosts

The Sersic profile, which is commonly used to model the surface brightness of a galaxy, is described by 3 fundamental parameters: the Sersic index n , the effective radius R_{eff} , and a normalization parameter. The stellar density profile can then be approximated by ([Prugniel & Simien 1997](#)):

$$\rho(r) = \rho_0 \left(\frac{r}{R_{\text{eff}}} \right)^{-p} e^{-b(r/R_{\text{eff}})^{1/n}} \quad (1)$$

$$p = 1 - \frac{0.6097}{n} + \frac{0.05563}{n^2} \quad (2)$$

$$b = 2n - \frac{1}{3} + \frac{0.009876}{n} \quad (3)$$

Here one can see that the stellar density profile is described with three independent parameters: 1) the effective radius R_{eff} ; 2) the Sersic inner slope, and p , which is a function of the Sersic index n and describes the steepness of the stellar density slope within R_{eff} ; and 3) the central stellar density ρ_0 , which is given by:

$$\rho_0 = \frac{M_\star}{4\pi R_{\text{eff}}^3} \frac{b^{n(3-p)}}{n \gamma_E(n(3-p))} \quad (4)$$

Here M_\star is the total stellar mass of the galaxy bulge/NSC or the cluster, and γ_E is the Euler Gamma function:

$$\gamma_E(x) = \int_0^\infty t^{x-1} e^{-t} dt \quad (5)$$

For the TDE rate calculation, the stellar density profile needs to be converted into the stellar distribution function (DF), which is the number density of stars as a function of the orbital specific energy E , using the Eddington formula:

$$f(E) = \frac{1}{\sqrt{8\pi^2 m}} \frac{d}{dE} \int_0^E \frac{d\rho}{d\psi} \frac{d\psi}{\sqrt{E-\psi}} \quad (6)$$

There is no analytic solution for the above equation, however, for the stellar profiles described by the Sersic profile. Therefore, we compute the DF numerically through PHASEFLOW ([Vasiliev 2017](#)), the details

of which are described in Section 2.5. We note that mathematically p has to be > 0.5 for the $f(E)$ to be positive. Hence, for systems with $p < 0.5$ we artificially replace p to be 0.5 when computing the DF.

2.2.2. King profile fits for NSCs

The King model is often used to describe globular clusters, and the density profile is given by:

$$\rho(\Psi) = \rho_1 \left[e^{\Psi/\sigma^2} \text{erf} \left(\frac{\sqrt{\Psi}}{\sigma} \right) - \sqrt{\frac{4\Psi}{\pi\sigma^2} \left(1 + \frac{2\Psi}{3\sigma^2} \right)} \right] \quad (7)$$

where ρ_1 is a scaling parameter, σ is the one-dimensional velocity dispersion, and Ψ is the relative gravitational potential between r and the tidal radius r_t :

$$\Psi(r) = \Phi(r_t) - \Phi(r) \quad (8)$$

The King model is parameterised by the king radius r_s and the dimensionless potential $W_0 \equiv \Psi(0)/\sigma^2$ ([King 1966](#)). We note that one could also parameterize the King model using the concentration parameter C instead of W_0 . For the IMBH-ON globular clusters with only C provided in the literature, we use the one-to-one correspondence between W_0 and C to obtain the value of W_0 ([Binney 2011](#)).

Since the King profile is basically a lowered isothermal model, its DF is similar to that of an isothermal sphere at small radii, but it is truncated at larger radii to have a finite mass. The DF for this profile has an analytic form ([Binney 2011](#)):

$$f(E) = \begin{cases} \frac{\rho_1}{(2\pi\sigma^2)^{3/2}} (e^{E/\sigma^2} - 1) & \text{when } E > 0 \\ 0 & \text{when } E < 0 \end{cases} \quad (9)$$

2.3. SMBH sample and host galaxy profiles

For comparison with IMBHs, we also utilize 37 SMBHs from nearby galaxies with their dynamically determined BH masses M_{BH} . These data are taken from [Davis et al. \(2019\)](#) who also provide Sersic profiles for the host galaxies. The TDE rates in these galaxies have been previously calculated by [Pfister et al. \(2020\)](#). We further select the BHs with masses between $10^6 - 10^8 M_\odot$ for our SMBH sample. A few of these galaxies with lower masses contain one or more NSC components. We follow [Pfister et al. \(2020\)](#) and adopt their NSC fit of the Milky Way, along with 2 other galaxies from [Pechetti et al. \(2022\)](#). The parameters of the SMBHs and their hosting galaxies are listed in Table A.3.

2.4. Loss Cone Dynamics

We provide a quick overview of the loss cone, but we refer readers to [Strubbe \(2011\)](#) and [Stone et al. \(2020\)](#) for a more in depth review. A star with mass m_* and radius r_* will be tidally disrupted by a massive black hole (MBH) of mass M_{BH} if it gets closer than the tidal disruption radius

$$r_t \equiv (M_{\text{BH}}/m_*)^{1/3} r_* \quad (10)$$

Specific orbital angular momentum of the star at r_t can be written as $L_{\text{lc}} = \sqrt{2GM_{\text{BH}}r_t}$. Hence, it can also be said that the star will get disrupted if its angular momentum $L < L_{\text{lc}}$. This phase space region is commonly known as the loss cone. We can further define a variable

$$R_{\text{lc}}(E) = \frac{L_{\text{lc}}^2}{L_{\text{circ}}^2(E)} = \frac{2GM_{\text{BH}}r_t}{L_{\text{circ}}^2(E)} \quad (11)$$

where $L_{\text{circ}}(E)$ is the specific angular momentum of a circular orbit.

Based on this variable and orbital period $P(E)$, we can define the loss cone filling factor such that:

$$q(E) = \frac{P(E)\bar{u}(E)}{R_{\text{lc}}(E)} \quad (12)$$

where $\bar{u}(E)$ is the orbital-averaged diffusion coefficient.

When $q \ll 1$, a star needs multiple orbital periods to be scattered into the loss cone and hence its orbit typically has a low β value. This constitutes the diffusive regime. On the opposite end, when $q \gg 1$, stars can scatter in and out the loss cone within a single orbital period and therefore their orbits can have any β , which enhances the probability of producing TDEs on deeply plunging orbits. This region is known as pinhole regime.

2.5. The TDE rate calculation

We mainly follow the approach of [Pfister et al. \(2020\)](#) to calculate TDE rates, which we briefly summarize below.

We start by utilizing PHASEFLOW ([Vasiliev 2017](#)), which takes the observed stellar profiles described by the Sersic or King model and returns a corresponding numerical DF. To be more specific, the following parameters are computed by PHASEFLOW:

- $\bar{f}(E)$ the averaged distribution function over angular momentum
- $\bar{u}(E)$ the orbital-averaged diffusion coefficient
- $L_{\text{circ}}(E)$ the angular momentum of a circular orbit of binding energy E
- $P(E)$ the orbital period

We then follow the prescriptions described in [Strubbe \(2011\)](#) to compute the TDE rates. The differential TDE rate can be computed using the following equation:

$$\frac{d^2\Gamma}{dEd \ln \beta} = -8\pi^2 GM_{\text{BH}} \frac{r_t}{\beta} \mathcal{G}(q(E), \beta), \quad (13)$$

where $\beta \equiv r_t/r_p$ is the penetration parameter defined by the ratio of the tidal disruption radius r_t and the pericenter radius r_p , and \mathcal{G} is given by the following equations:

$$\mathcal{G}(q, \beta) = \frac{\bar{f}(E)}{1 + q^{-1}\xi(q) \ln(1/R_{\text{lc}})} \left[1 - 2 \sum_{m=1}^{\infty} \frac{e^{-\alpha_m^2 q/4}}{\alpha_m} \frac{J_0(\alpha_m \beta^{-1/2})}{J_1(\alpha_m)} \right] \quad (14)$$

$$\xi(q) = 1 - 4 \sum_{m=1}^{\infty} \frac{e^{-\alpha_m^2 q/4}}{\alpha_m^2} \quad (15)$$

Here, J_i is the Bessel function of i^{th} -order, and a_m is the m^{th} zero of J_0 .

2.6. Stellar mass function for disrupted stars

In this work, we take the mass distribution of stars $\phi(m)$ explicitly into account instead of using a monochromatic stellar mass as done by previous groups. We use the Kroupa initial mass function (IMF) with the stellar mass $m \in [0.08, 10]$, which has the form ([Kroupa 2001](#)):

$$\phi(m) \propto \begin{cases} m^{-1.3} & \text{for } m < 0.5 \\ m^{-2.3} & \text{for } m > 0.5 \end{cases} \quad (16)$$

For a distribution of stellar masses, we have the total differential TDE rate to be:

$$\frac{d^2\Gamma}{dEd \ln \beta} = \int \frac{d^2\Gamma(m)}{dEd \ln \beta} m \phi(m) d \ln m \quad (17)$$

For computing the above, we use $f = f_{\text{mono}}/\langle m \rangle$ and $\bar{u} = \bar{u}_{\text{mono}}\langle m^2 \rangle/\langle m \rangle$, where f_{mono} and μ_{mono} are the the DF and diffusion coefficient of a monochromatic stellar mass distribution as described in Section 2.5 (see the derivation of these two equations in Appendix B), $\langle m \rangle = \int m \phi(m) dm$ is the averaged mass of stars, and $\langle m^2 \rangle = \int m^2 \phi(m) dm$ is the mean-square of the stellar mass distribution.

3. RESULTS

3.1. TDE rates from IMBHs and SMBHs

We calculate TDE rates following the method outlined in Section 2.5. The TDE rates from IMBH-GNs and

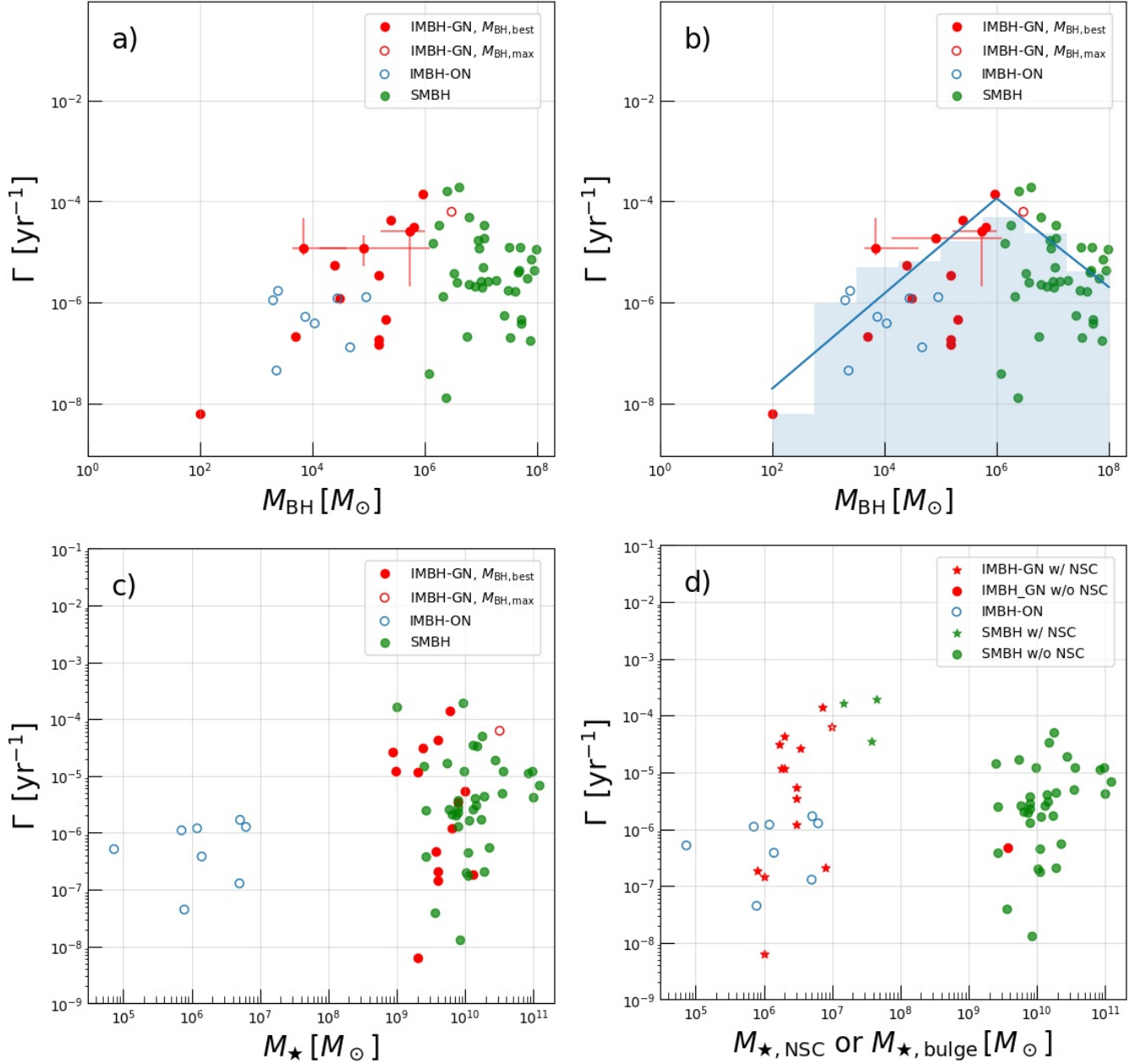


Figure 1. TDE rate Γ for each galaxy or cluster in our sample. Three different populations of MBHs are shown denoted using different colors: all IMBH-GNs in red, all IMBH-GCs in blue, and all SMBHs in green. Panel (a) shows Γ plotted against M_{BH} . We adopt $M_{\text{BH}, \text{best}}$ (solid symbol) for a MBH if an accurate mass measurement exists, otherwise use $M_{\text{BH}, \text{max}}$ (empty symbol) if only a tentative measurement exists. Panel (b) is the same as (a) but includes additional histograms (blue shaded regions) showing the averaged TDE rate distribution and a broken power-law fit (blue line) for the averaged $\Gamma - M_{\text{BH}}$ relation (Eqn. 18). One can see that Γ increases with M_{BH} in the IMBH regime but decreases with M_{BH} in the SMBH regime. Panel (c) shows Γ plotted against the total stellar mass of a galaxy or cluster M_{\star} . Panel (d) shows Γ plotted against the mass of the innermost stellar component when a galaxy can be fitted with multiple components. Galaxies with a NSC as the innermost component are represented using star symbols instead of circles.

IMBH-ONs compared to those computed from SMBHs are plotted in Fig. 1.

In Fig. 1, panel (a) shows the TDE rates Γ from individual galaxies or clusters plotted against M_{BH} . For the IMBH population studied here, we denote the rates computed with $M_{\text{BH,best}}$ or $M_{\text{BH,max}}$ using solid or empty symbols respectively and different colors for the IMBH-GN TDEs (red); IMBH-ON TDEs (blue), and all SMBH TDEs (green). For galaxies that are fitted with more than one component, the TDE rates from these components are summed together, although we note that the innermost NSC dominates the rate calculation. Overall, the TDE rates from IMBHs range between $\sim 10^{-8} - 10^{-4} \text{ gal}^{-1} \text{ yr}^{-1}$, which is comparable to those from SMBHs. One can see that Γ increases with M_{BH} in the IMBH regime but decreases with M_{BH} in the SMBH regime. These strikingly opposite trends of Γ v.s. M_{BH} in the IMBH and SMBH regimes are seen. For SMBHs, Γ on average decreases as M_{BH} increases, which is qualitatively consistent with earlier results from Wang & Merritt (2004), Stone & Metzger (2016), and Pfister et al. (2020). However, we find that for the population of IMBHs, Γ generally increases with increasing M_{BH} . On average, the TDE rate peaks around $M_{\text{BH}} \sim 10^6 M_{\odot}$. This turnover in TDE rate as a function of M_{BH} is qualitatively consistent with the results by Polkas et al. (2023). They suspect that this behavior is a consequence of the remarkably different stellar profiles of NSCs and bulges. We conduct a further investigation on the cause of this turnover in Section 3.6.

We next calculate the averaged TDE rate Γ as a function of M_{BH} in Fig. 1 panel (b). Based on the individual galaxy/cluster TDE rate shown in panel (a), we make histograms of averaged TDE rates in each M_{BH} bin, which are now shown as the blue shaded regions in panel (b). For this calculation the samples with tentative M_{BH} measurements are down-weighted by half. It is clearly seen that the averaged TDE rate in a M_{BH} bin is dominated by galaxies with higher TDE rates. Then we fit the histograms to obtain the $\Gamma - M_{\text{BH}}$ with a broken power-law function, with the turnover placed at $M_{\text{BH}} = 10^6 M_{\odot}$. The best-fit functions plotted using blue lines) are:

$$\Gamma = \begin{cases} 1.2 \times 10^{-4} \left(\frac{M_{\text{BH}}}{10^6 M_{\odot}} \right)^{0.9} \text{ yr}^{-1} & \text{for } M_{\text{BH}} \leq 10^6 M_{\odot} \\ 1.2 \times 10^{-4} \left(\frac{M_{\text{BH}}}{10^6 M_{\odot}} \right)^{-0.9} \text{ yr}^{-1} & \text{for } M_{\text{BH}} > 10^6 M_{\odot} \end{cases} \quad (18)$$

We now plot the TDE rates for IMBHs and SMBHs against the total stellar mass M_{\star} of the host galaxy or cluster in Fig. 1 panel (c). We see that there exists a

clear gap in the stellar mass between clusters hosting IMBH-ONs and the others. Some of the galaxies hosting IMBH-GNs are considered dwarf galaxies with total stellar masses $M_{\star} < 3 \times 10^9 M_{\odot}$. However, surprisingly, most galaxies hosting IMBH-GNs have stellar masses that are larger, in fact, they are only slightly smaller than those of galaxies hosting SMBHs. This indicates that the M_{BH} scaling relations for SMBHs likely breaks down for IMBHs. This we note is consistent with previous findings (Greene & Ho 2006; Martín-Navarro & Mezcua 2018). Additionally, the majority of our sample of galaxies hosting IMBHs, do contain dense NSCs. Therefore, we also plot the TDE rate against the mass of the innermost stellar component in Fig. 1 panel (d). Here we denote the innermost stellar component of a galaxy using a star symbol if it is a NSC or continue using a circle if it is a bulge. Most galaxies hosting IMBH-GNs have NSCs in the center, whereas most galaxies hosting SMBHs only have bulges. However, it is not straightforward to infer the IMBH TDE rates using either the total stellar mass or the stellar mass of the innermost stellar component.

Last but not least, we note that generally the IMBH mass determinations bear a larger degree of uncertainty compared to those of SMBHs. This leads to higher uncertainties in the IMBH TDE rate estimates. Furthermore, the choice of the stellar profile model can lead to discrepancies in the TDE rate estimates. While we have used the Sersic stellar density profiles for calculating the TDE rates from IMBH-GNs and SMBHs, the clusters hosting IMBH-ONs are only described with the King model in the literature. However, the effect of this discrepancy tends to be small and the difference in rate estimates is usually within 0.5 dex (Stone & Metzger 2016). This implies that to first order, our results and inferred trends are trust-worthy and reliable.

3.2. The TDE pinhole fraction

The TDE pinhole fraction f denotes the fraction of TDEs in the pinhole regime:

$$f \equiv \frac{\Gamma_{q>1}}{\Gamma_{\text{tot}}} \quad (19)$$

where $\Gamma_{q>1}$ denotes the rate of TDEs with $q > 1$, and Γ_{tot} denotes the total TDE rate. We calculate f for all three populations studied here: IMBH-GNs, IMBH-ONs, and SMBHs, and plot f vs. M_{BH} and f vs. M_{\star} in Fig. 2. For SMBHs we see that on average f decreases as M_{BH} increases. This is consistent with the result reported earlier in Stone & Metzger (2016). Interestingly, for both IMBH-GNs and IMBH-ONs, f generally stays close to unity regardless of M_{BH} . This means that

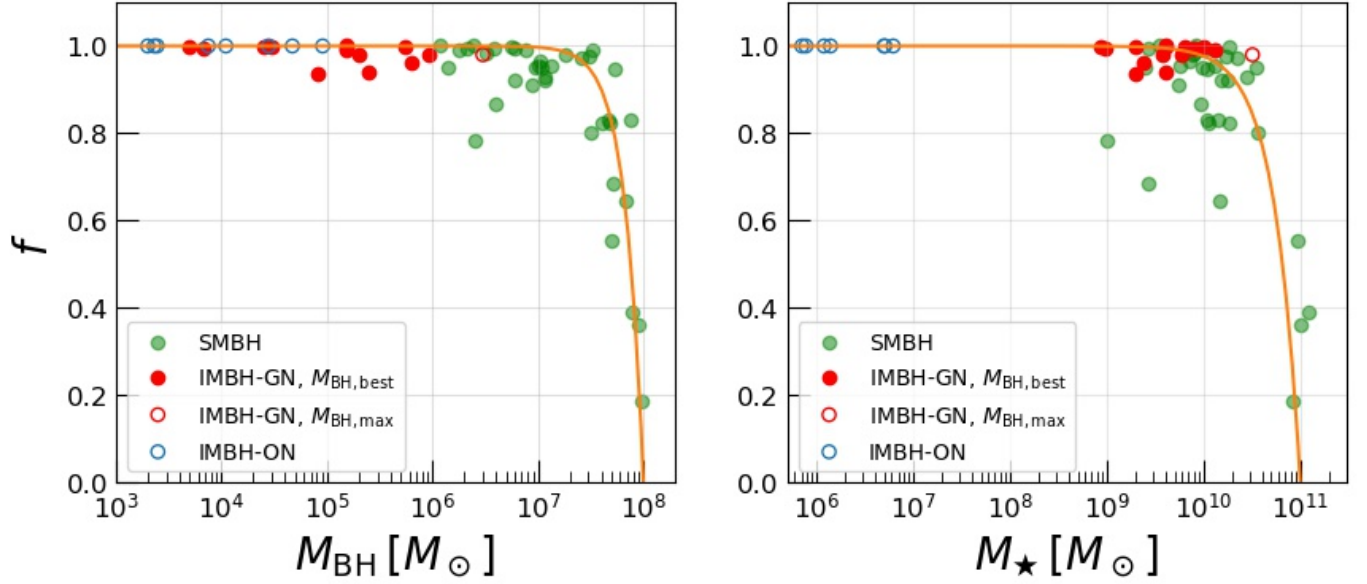


Figure 2. Pinhole fraction f plotted against M_{BH} and M_{\star} . The symbols and colors are the same as in Fig. 1. The orange curves represent the fitting functions (Eqn. 20 & 21).

IMBH TDEs mostly reside in the pinhole regime. Even for SMBHs, TDEs only start to be mainly in the diffusive regime when M_{BH} becomes large enough. A similar trend with M_{\star} is also found and shown.

The relation between f and M_{BH} is determined by multiple physical factors. If one keeps the stellar profile the same but varies M_{BH} , it is found that a larger M_{BH} will lead to a lower f . There are two reasons for this. First, increasing M_{BH} moves the tidal disruption radius r_T closer to the black hole event horizon. Second, the loss cone size also increases with M_{BH} . Both these effects cohere to increase the fraction of TDEs in the diffusive regime. This is explained in more detail in Appendix C and illustrated with the case of NGC1042. Furthermore, f depends on the stellar density profile, which has an implicit dependence on M_{BH} , which we address in the next section.

We provide the following fitting functions for f vs. M_{BH} and f vs. M_{\star} :

$$f(M_{\text{BH}}) = 1 - \left(\frac{M_{\text{BH}}}{10^8 M_{\odot}} \right)^{2.5} \quad (20)$$

$$f(M_{\star}) = 1 - \left(\frac{M_{\star}}{10^{11} M_{\odot}} \right)^{1.6} \quad (21)$$

3.3. Impact of the stellar profile of the host galaxy or cluster

In this section, we investigate how the stellar density profiles of IMBH/SMBH host galaxies or clusters af-

fect their TDE rates and pinhole fractions. As a reminder, the stellar profiles of galaxies hosting SMBHs and IMBH-GNs in our sample are modeled using the Sersic profile, which is described by three fundamental parameters (Eqn. 1-4): 1) the Sersic inner slope p , 2) the stellar central density ρ_0 , and 3) the effective radius R_{eff} . Clusters hosting IMBH-ONs in our sample are only modelled using the King profile.

We plot the stellar density profiles $\rho(r)$ of all galaxies or clusters hosting IMBH-GNs (Table A.1) and IMBH-ONs (Table A.2) in Fig. 3 panel (a) and (b), respectively, using solid curves. For comparison, we also calculate the mean and the standard deviation σ of $\rho(r)$ for all SMBH-hosting galaxies (Table A.3), and show the 1- σ range of the mean value using the blue shaded region. In general, the galaxies hosting IMBH-GNs appear to have higher stellar central densities, similar inner density slopes, and smaller effective sizes compared to the galaxies hosting SMBHs. On the other hand, the clusters hosting IMBH-ONs appear to have similar stellar central densities, steeper stellar density slopes, and smaller sizes compared to galaxies hosting SMBHs.

We next investigate the implicit relations between the black hole mass and host galaxy/cluster stellar profiles in our sample. We plot M_{BH} vs. p , M_{BH} vs. ρ_0 and M_{BH} vs. R_{eff} in Fig. 4 panels (a)-(c) respectively for IMBH-GNs and SMBHs in our sample. We exclude IMBH-ONs from these plots as the x-axis parameters are relevant only for the Sersic model. For galaxies with both bulge and NSC components, we only use the parameters of the innermost NSC component and indicate that using

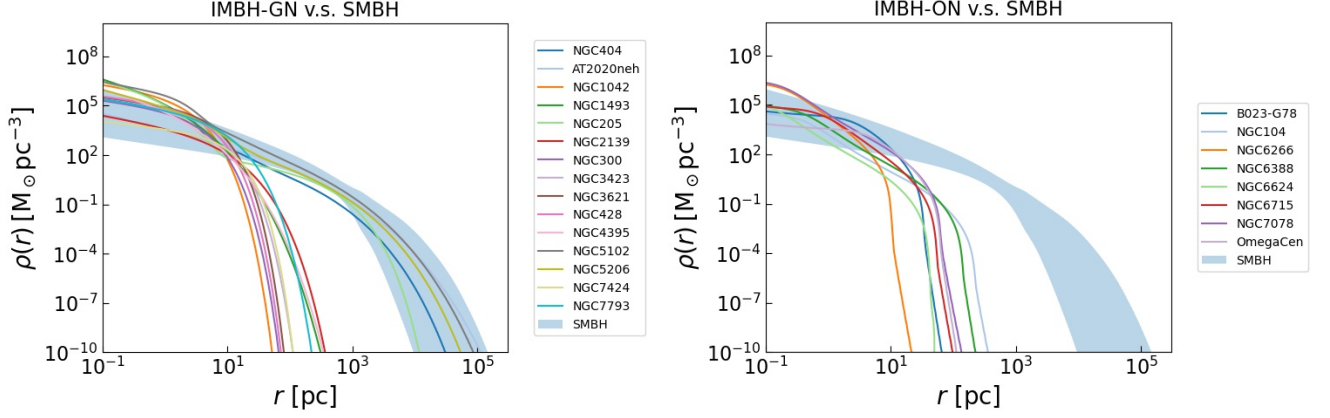


Figure 3. The stellar density profiles of galaxies and clusters hosting IMBH-GNs (left panel) and IMBH-ONs (right panel). The shaded region shows the 1- σ range of the stellar density profiles of the galaxies hosting SMBHs for comparison.

star symbols. The stellar profile parameter comparisons between IMBH-GNs and SMBHs hosts are consistent with Fig. 3 panel (a). IMBH-GN host galaxies have higher central stellar densities since they all have NSC components. Their stellar density slopes are on average similar to that of SMBH hosts. Furthermore, the R_{eff} of the innermost NSCs in both IMBH-GN and SMBH hosts are generally quite compact, with R_{eff} ranging mostly between $10^0 - 10^1$ pc. The NSC size does not appear to correlate with M_{BH} . On the other hand, the bulges of galaxies hosting SMBHs have larger sizes ($R_{\text{eff}} > 10^2$ pc), and the bulge size generally increases with M_{BH} .

We also plot the correlation between the TDE rate from each galaxy and the respective stellar profile parameters: Γ vs. p , Γ vs. ρ_0 and Γ vs. R_{eff} , in Fig. 4 panels (d)-(f). Fig. 4 panel (d) shows that Γ generally increases with the inner slope p for both populations, although a large scatter is seen. This can be interpreted as follows: a steeper p puts more stars closer to the MBH, increasing the probability of scattering stars into the loss cone and hence enhancing the TDE rate. The Γ vs. p relations for IMBH-GNs and SMBHs can be fit with the following power-law functions respectively:

$$\Gamma = \begin{cases} 2.9 \times 10^{-10} 10^{7p} & \text{yr}^{-1} \text{ for IMBH-GNs} \\ 3.2 \times 10^{-8} 10^{3p} & \text{yr}^{-1} \text{ for SMBHs} \end{cases} \quad (22)$$

Fig. 4 panel (e) shows a clear positive correlation between Γ and ρ_0 for each population. This is not surprising – it is expected that the TDE rate should scale with the overall stellar density as there are more stars available for disruption. Once again, we see very similar trends in the Γ vs. ρ_0 relations for IMBH-GNs and SMBHs, albeit with a small offset. The best-fit power-law relations are:

$$\Gamma = \begin{cases} 9.3 \times 10^{-8} \rho_0^{0.7} & \text{yr}^{-1} \text{ for IMBH-GNs} \\ 3.0 \times 10^{-9} \rho_0^{0.7} & \text{yr}^{-1} \text{ for SMBHs} \end{cases} \quad (23)$$

On the other hand, Fig. 4 panel (f) shows that R_{eff} does not affect Γ .

Lastly, we show how the TDE pinhole fraction f in each galaxy depends on the stellar density parameters: f vs. p , f vs. ρ_0 and f vs. R_{eff} , in Fig. 4 panel (g)-(i), respectively. Here the SMBH population is further split into two groups according to their masses: $10^6 - 10^7 M_{\odot}$ (turquoise dots) and $> 10^7 M_{\odot}$ (orange dots). One can see that p is the most important parameter determining f : f typically decreases with increasing p . When p is below ~ 0.7 , f is approximately unity. Once $p \gtrsim 0.7$, f gradually decreases toward 0. To understand how p impacts f , one can imagine a galaxy with a very flat inner density slope (i.e., with very small p). In such a hypothetical scenario, more stars are further from the MBH, so more energetic scatterings will be required for stars to enter the loss cone, i.e., more TDEs will be disrupted in the pinhole regime. Interestingly, we also find that all galaxies with low- f and high- p values host heavy SMBHs with $M_{\text{BH}} > 10^7 M_{\odot}$. Since stars are more likely disrupted by lighter MBHs, this means that the majority of TDEs should occur in the pinhole regime.

The dependence of f on ρ_0 or R_{eff} is more subtle. From Fig. 4 panel (h) no obvious trend is seen when looking at all the galaxy populations in concert. This is expected since ρ_0 is only a scaling factor for the stellar density which does not affect f . However, after decomposing the galaxy populations into three categories: IMBHs, lighter SMBHs, and heavier SMBHs, it is seen that f decreases with increasing ρ_0 for each galaxy population. This is because when we fix the range of M_{BH} , we somewhat confine the range of M_{\star} to wherein a larger ρ_0 would result in a larger p . As for Fig. 4 panel (i), we do not notice any obvious, direct trend between f and R_{eff} .

In summary, there exist positive correlations between the TDE rate and two stellar density profile parameters,

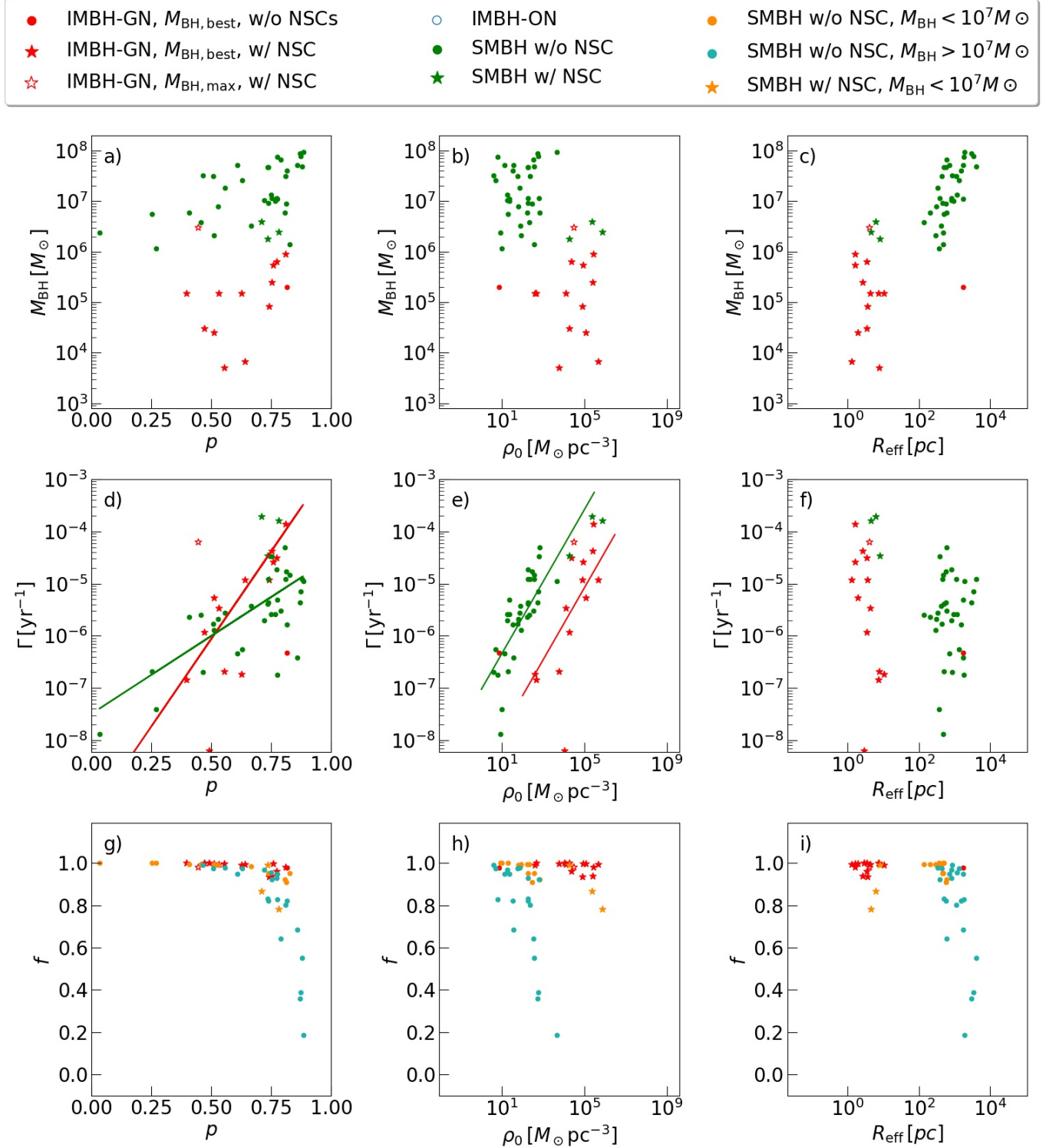


Figure 4. MBH mass M_{BH} , individual galaxy TDE rate Γ , TDE pinhole fraction f (from top to bottom) plotted against the Sersic inner slope p , central density ρ_0 and effective radius R_{eff} (from left to right) for our IMBH and SMBH samples. The symbol style and colors are consistent with Fig. 1 panel (d), except in panels (g), (h) and (i) where the SMBHs are further divided into two sub-groups: $M_{\text{BH}} > 10^7 M_{\odot}$ (turquoise) and $10^6 M_{\odot} < M_{\text{BH}} < 10^7 M_{\odot}$ (orange). In panels (d) and (e), the red and green lines also display the fitting functions (Eqn. 22 and 23) for IMBH-GN hosts and SMBH hosts respectively.

ρ_0 and p , separately for the IMBH-GN and SMBH populations. On the other hand, the TDE pinhole fraction f primarily depends on p . However, there exist implicit relationships between these parameters when we consider a specific MBH mass range. For example, almost all host IMBH-GNs and SMBHs with $M_{\text{BH}} < 10^7 M_{\odot}$ in our sample have stellar profiles with $p \lesssim 0.7$, which means the TDEs from these systems mostly occur in the pinhole regime.

3.4. Volumetric Rates of IMBH and SMBH TDEs

In this section we compute the volumetric TDE rates for IMBHs and SMBHs. The volumetric rate \dot{N} is computed as follows:

$$\dot{N}(M_{\text{BH}}) = \Phi(M_{\text{BH}}) \cdot \Gamma(M_{\text{BH}}) \quad (24)$$

Here $\Gamma(M_{\text{BH}})$ is the TDE rate per galaxy (in the unit of $\text{yr}^{-1} \text{gal}^{-1}$) as a function of M_{BH} based on the histograms in Fig. 1 (b), and $\Phi(M_{\text{BH}})$ is the BH mass function (BHMF) fit. We adapt the BHMF from Gallo & Sesana (2019), for which Wong et al. 2022 has provided a more precise formula:

$$\log_{10} \left(\frac{\Phi_{\text{BH}}}{\text{Mpc}^{-3} M_{\odot}^{-1}} \right) = -9.82 - 1.1 \times \log_{10} \left(\frac{M_{\text{BH}}}{10^7 M_{\odot}} \right) - \left(\frac{M_{\text{BH}}}{128 \times 10^7 M_{\odot}} \right)^{1/\ln(10)} \quad (25)$$

The results are shown in Fig. 5. Unsurprisingly, the volumetric TDE rate first increases with M_{BH} until $M_{\text{BH}} \sim 10^6 M_{\odot}$ and then drops as M_{BH} further increases. We fit the averaged volumetric TDE rate using a broken power-law function, with the break point set again at $M_{\text{BH}} = 10^6 M_{\odot}$:

$$\dot{N} = \begin{cases} 2.9 \times 10^{-7} \left(\frac{M_{\text{BH}}}{10^6 M_{\odot}} \right)^{0.8} & \text{yr}^{-1} \text{Mpc}^{-3} \text{dex}^{-1} \\ & \text{when } M_{\text{BH}} \leq 10^6 M_{\odot} \\ 2.9 \times 10^{-7} \left(\frac{M_{\text{BH}}}{10^6 M_{\odot}} \right)^{-1.2} & \text{yr}^{-1} \text{Mpc}^{-3} \text{dex}^{-1} \\ & \text{when } M_{\text{BH}} > 10^6 M_{\odot} \end{cases} \quad (26)$$

For each MBH population, the total volumetric TDE rate is estimated to be around $3 \times 10^{-7} \text{Mpc}^{-3} \text{yr}^{-1}$ (IMBH-GNs), $7 \times 10^{-9} \text{Mpc}^{-3} \text{yr}^{-1}$ (IMBH-ONs), and $9 \times 10^{-8} \text{Mpc}^{-3} \text{yr}^{-1}$ (SMBHs).

One can also compare these theoretical TDE rates with the observed rates, although we note that there is a large discrepancy in the latter as reported in the

literature. For example, van Velzen & Farrar (2014) calculated the TDE rates based on surveys from SDSS and Pan-STARRS and obtained a volumetric rate of $10^{-8} \text{Mpc}^{-3} \text{yr}^{-1}$ for TDEs around SMBHs. In later work, van Velzen (2018) combined more surveys including GALEX, PTF, iPTF, and ASAS-SN, and updated this number upward to be $5 \times 10^{-7} \text{Mpc}^{-3} \text{yr}^{-1}$. On the forefront of IMBH-TDE observations, Lin et al. (2018) reported an off-center TDE candidate J2150-0551 from an IMBH with mass between $5 \times 10^4 - 10^5 M_{\odot}$ found by searching the 3XMM-DR5 catalog, and from this estimated the IMBH-TDE volumetric rate to be $\sim 10^{-8} \text{Mpc}^{-3} \text{yr}^{-1}$. Moreover, the Young Supernova Experiment released its first set of data (YSE DR1) that includes 5 TDEs (Aleo et al. 2023), of which AT2020neh is of particular interest as it was found to be in the vicinity of an IMBH with M_{BH} ranging between $10^{4.7} - 10^{5.9} M_{\odot}$ (Angus et al. 2022). Based on this, the estimated IMBH-TDE rate is $\lesssim 2 \times 10^{-8} \text{Mpc}^{-3} \text{yr}^{-1}$. Very recently, Yao et al. (2023) also reported a TDE rate of $\sim 3 \times 10^{-7} \text{Mpc}^{-3} \text{yr}^{-1}$ using 33 optical selected TDEs from the Zwicky-Transient Facility, with M_{BH} ranges from $10^{5.1}$ to $10^{8.2} M_{\odot}$. TDE rate determinations from larger samples are needed to settle the issue.

We have compiled the more recent observed TDE rate estimates mentioned above in Fig. 5. While our theoretical rates and the observed rates of TDEs seem roughly in good agreement, we caution that there are uncertainties in both the observed and theoretical TDE rates. Factors such as selection effect, instrumentation bias, and obscuration should systematically lower the chance of observing a TDE. Furthermore, current transient surveys might not catch all IMBH-TDEs, which reside off-center in massive galaxies or have non-typical flaring evolution timescales (Chen & Shen 2018; Pfister et al. 2022). The upshot is that the true TDE rate is likely somewhat higher than the observed rate, and the values reported should be interpreted as a lower limit instead. On the theoretical side, multiple factors also contribute to the uncertainties in the TDE rate calculation. One that is widely debated is the occupation fraction of IMBHs in galaxies, which is expected to vary as a function of epoch and host galaxy mass. The BHMF we used in this work is based on Gallo & Sesana (2019), which has a 2σ -uncertainty of $\sim \pm 1$ dex for IMBHs. We also note that this BMMF is based on AGN observations, and does not include IMBHs in GCs. Since every massive galaxy can possibly host several GCs, we have likely underestimated the rates of off-center IMBH TDEs. Moreover, the IMBH mass estimates also bear huge uncertainties, with the differences between the best and maximum M_{BH} estimates reaching as high as 3

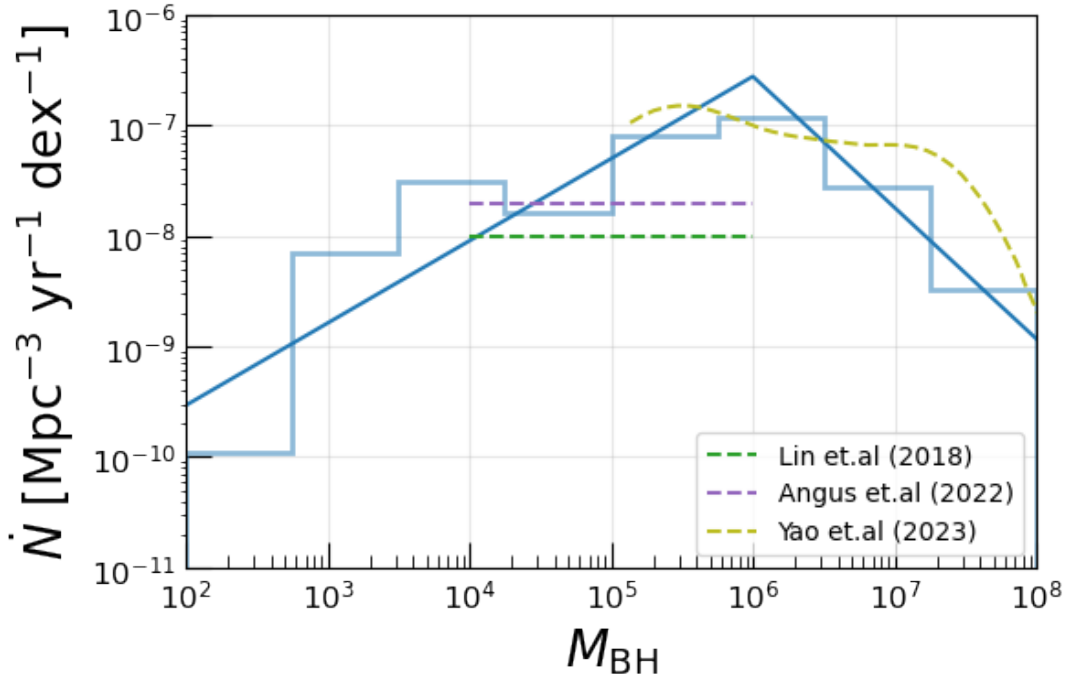


Figure 5. The volumetric TDE rate \dot{N} v.s. M_{BH} . The blue histogram in this plot is obtained from convolving the histogram in Fig. 1 (b) with the BHMF from Gallo & Sesana (2019). The blue line shows the fitting function (Eqn. 26). Comparison to observations is also shown using dashed lines: Lin et al. (2018) and Angus et al. (2022) reported volumetric IMBH-TDE rates of $\sim 10^{-8} \text{Mpc}^{-3} \text{yr}^{-1}$ based on the observation of J2150-055 and AT2020neh respectively, and Yao et al. (2023) reported volumetric TDE rate as a function of M_{BH} based on the 33 optically selected ZTF TDEs.

dex. Last but not least, TDE physics plays an important role so that when comparing theoretical and observed rates, it may turn out that some events might not produce bright or prompt flares (Kochanek 2016; Wong et al. 2022). For example, Wong et al. (2022) considered disk formation physics and reported that TDEs around less massive BHs are likely to go through slow disk formation, which will make the flare evolve on longer timescales and lower the chance of their detection given our current observational strategies.

3.5. The distribution of the penetration parameter β

In this section, we calculate the distribution of the penetration parameter β for both IMBH and SMBH TDEs. The probability density function of β is calculated as follows:

$$\frac{dP}{d\beta} = \frac{1}{\beta\Gamma} \int \frac{d^2\Gamma}{dE d\ln\beta} dE \quad (27)$$

We show the results in Fig. 6 for our IMBH and SMBH samples. The curves are color-coded by the values of M_{BH} , which goes from green ($10^{7-8} M_{\odot}$) to red ($10^{4-5} M_{\odot}$).

The IMBH TDEs and SMBH TDEs with $M_{\text{BH}} \lesssim 10^7 M_{\odot}$ have β -distributions that largely follow $dP/d\beta \propto \beta^{-2}$, which is consistent with the pinhole-dominated regime. The curves start to drop at very large β where

the smallest/densest stars need to get within the BH event horizon before they are disrupted, and eventually cut off for when the biggest/least dense stars also plunge into the BH before being disrupted. On the other hand, when $M_{\text{BH}} \gtrsim 10^7 M_{\odot}$, the β -distribution is steeper, indicating that some fraction of TDEs can also be produced in the diffusive regime.

Interestingly, TDEs from IMBHs can have β as high as $\sim 100 - 1000$. This is very different from what is expected for SMBH TDEs for which β can only reach to around 10. Observationally, it has been reported that very high β might cause the flare rise time to become longer (Guillochon & Ramirez-Ruiz 2013). In an extreme case, it has been argued the compression experienced by a very deeply-plunging star might even be strong enough to trigger nuclear burning, and the explosion induced can resemble a Type Ia supernovae and produce unique signatures (Rosswog et al. 2009).

3.6. A detailed investigation on how BH mass and galaxy stellar profile affect the TDE rate

We delve deeper to investigate the behavior of the TDE rate Γ computed from individual galaxies as a function of M_{BH} described in Section 3.1 and seek to understand the cause for the Γ v.s. M_{BH} trend as shown in Fig. 1 panel (b). To explore this, we first compute the TDE

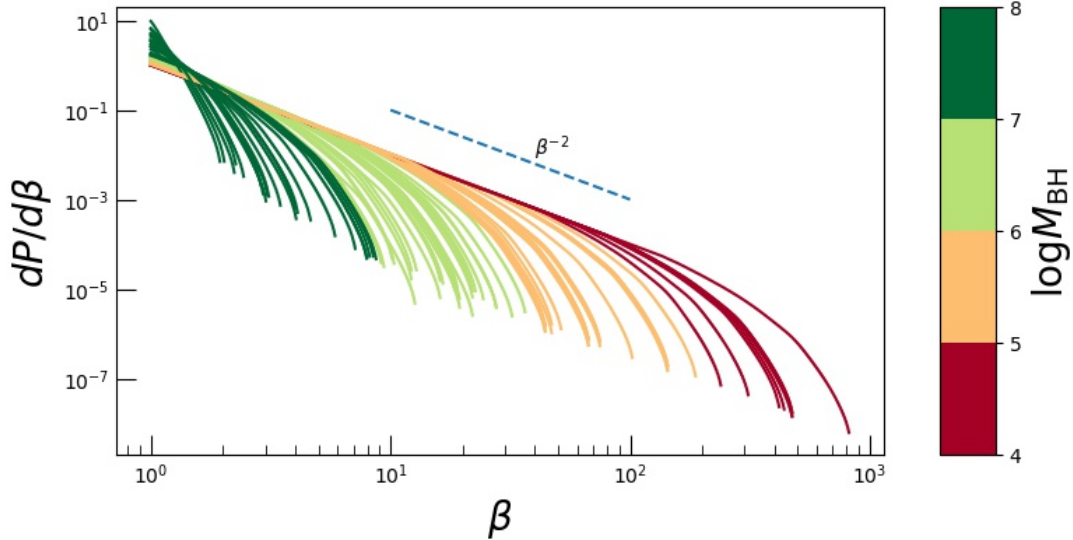


Figure 6. The distribution of penetration parameter β in TDEs for different M_{BH} . The curves are color coded by M_{BH} , from $10^8 M_{\odot}$ (green) to $10^4 M_{\odot}$ (red). The dashed line denotes the $dP/d\beta \propto \beta^{-2}$ relation that characterizes the pinhole dominated regime.

rate for each galaxy or cluster by varying M_{BH} as a free parameter over a range of $10^3 M_{\odot} - 10^8 M_{\odot}$ while keeping the galaxy stellar profiles fixed as dictated by observations. The Γ v.s. M_{BH} results for IMBHs and SMBHs are presented in Fig. 7, where the curves show the fit using a 3rd degree polynomial. Interestingly, for almost all galaxies in our sample, Γ from each galaxy exhibits a similar behavior, in that it first increases with M_{BH} and then turns over at a certain M_{BH} , after which Γ reverses and starts to decrease with M_{BH} .

We further examine the value of the optimal BH mass ($M_{\text{BH,peak}}$) at which the $\Gamma(M_{\text{BH}})$ curve reaches maximum and compare that to the actual observed BH mass ($M_{\text{BH,obs}}$) for each galaxy. Fig. 8 shows the difference between these two masses ($\Delta \log M_{\text{BH}} \equiv \log M_{\text{BH,peak}} - \log M_{\text{BH,obs}}$) as a function of $\log M_{\text{BH,obs}}$. We see a monotonically decreasing trend between $\Delta \log M_{\text{BH}}$ and $\log M_{\text{BH,obs}}$, and the sign of $\Delta \log M_{\text{BH}}$ switches at around a few times $10^6 M_{\odot}$. This, again, demonstrates that $\Gamma(M_{\text{BH}})$ should itself on average also peak around $10^6 M_{\odot}$ for the galaxies/clusters in our sample.

Next, we check how the galaxy stellar profile affects the computation of $\Gamma(M_{\text{BH}})$. We plot $d \log \Gamma / d \log M_{\text{BH}}$ against the Sersic inner slope p for each galaxy in Fig. 9. Here $d \log \Gamma / d \log M_{\text{BH}}$ is the slope of $\Gamma(M_{\text{BH}})$ calculated at the observed BH mass $M_{\text{BH,obs}}$. On average, we find that $d \log \Gamma / d \log M_{\text{BH}}$ decreases with p (although some scatter exists), which is consistent with the results in Wang & Merritt (2004). Around a value of $p \sim 0.6$, the sign of $d \log \Gamma / d \log M_{\text{BH}}$ switches from positive to negative. This means that when the stellar component is less centrally concentrated (lower value of p), $\Gamma(M_{\text{BH}})$

tends to increase with M_{BH} , and most IMBH-GN hosts reside within this regime. On the other hand, for a more centrally concentrated stellar component (higher value of p), $\Gamma(M_{\text{BH}})$ more likely decreases with M_{BH} . Our SMBH host population roughly splits between these two p -regimes.

Finally, we investigate how the effective size R_{eff} of the innermost stellar component of a galaxy affects Γ . To be more specific, in Fig. 10 we plot the ratio between the BH influence radius r_{inf} and the effective radius of the inner stellar component R_{eff} against M_{BH} . Interestingly, the trend of this ratio also somewhat resembles the trend seen in Γ vs. M_{BH} (Fig. 1 panel (b)): $r_{\text{inf}}/R_{\text{eff}}$ initially increases with M_{BH} at low M_{BH} and then decreases with M_{BH} at high M_{BH} with a turnover at around $\sim 10^6 M_{\odot}$. We take a closer look at this behavior and offer the following explanation: 1) In the IMBH mass range, as M_{BH} increases, r_{inf} also increases, while R_{eff} of the NSCs does not vary much (as shown in Fig. 4 panel (c)); a larger r_{inf} therefore puts more stars within the gravitational influence of the BH, which enhances the TDE rate; 2) r_{inf} becomes comparable to R_{eff} around $M_{\text{BH}} = 10^6 M_{\odot}$, the mass scale that separates our IMBH and SMBH populations. Beyond this M_{BH} , r_{inf} still increases with M_{BH} . However, the R_{eff} of SMBH galaxy bulges are much larger than the sizes of the compact NSCs, so $r_{\text{inf}}/R_{\text{eff}}$ overall drops to lower values. A lower $r_{\text{inf}}/R_{\text{eff}}$ means that the stars are more spread out (compared to the sphere of influence of the BH), which then decreases the TDE rate.

The only outlier in Fig. 10 is AT2020neh, for which only a bulge component of the host galaxy has been re-

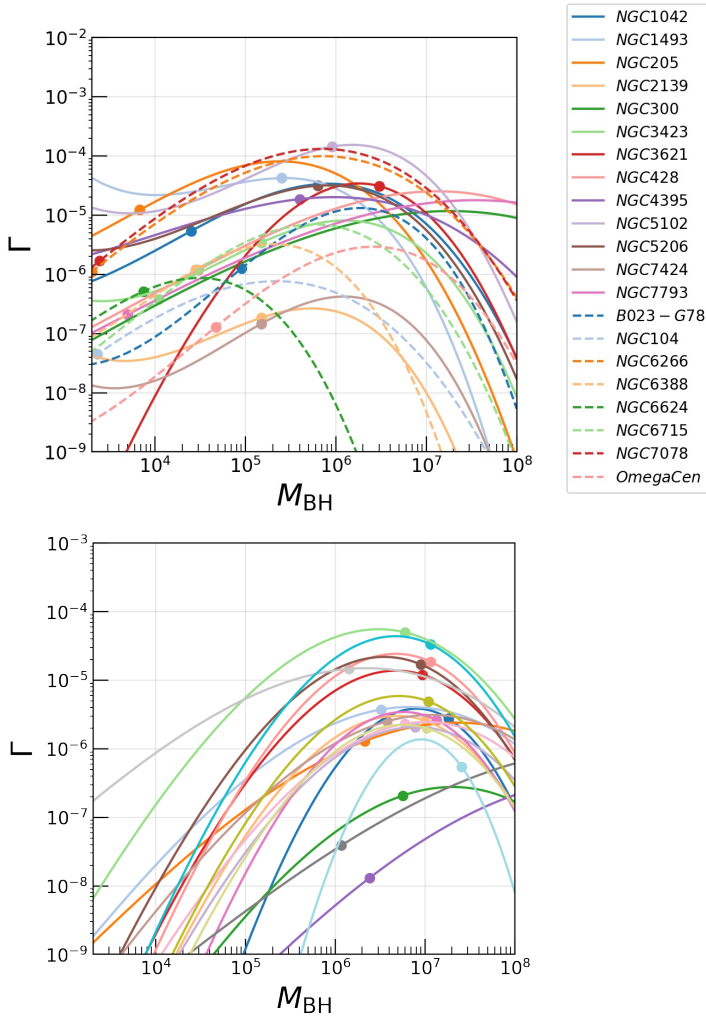


Figure 7. TDE rate Γ from each galaxy or cluster as a function of M_{BH} (while keeping the stellar profiles fixed) from IMBHs (top panel) and SMBHs (bottom panel). Solid lines and dotted lines in the top panel represent IMBH-GNs and IMBH-ONs respectively. The dots mark the observed BH masses $M_{\text{BH,obs}}$ and the corresponding TDE rates.

ported in literature. Hence the R_{eff} used here is large and $r_{\text{inf}}/R_{\text{eff}}$ is very small. We suspect that it is however, possible that the host galaxy of AT2020neh could host NSCs as well, like most IMBH-hosting galaxies. However, the galaxy is too far (at $d = 0.45 - 0.9\text{kpc}$) for the NSCs to be resolved observationally.

In summary, we conclude that the opposite trend of Γ v.s. M_{BH} seen in the IMBH population to that of the SMBH population is a result of a combination of factors. For most realistically observed stellar profiles, $\Gamma(M_{\text{BH}})$ peaks around the sweet spot of $M_{\text{BH}} \sim 10^6 M_{\odot}$. Also, the stellar components of the IMBH and SMBH host galaxies are structured differently in terms of both p and

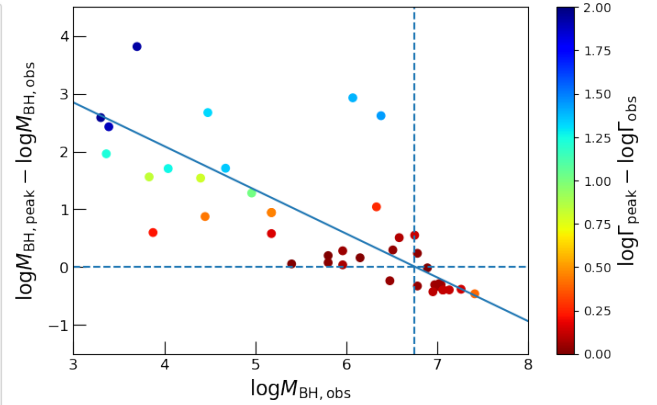


Figure 8. The difference between the observed BH mass $M_{\text{BH,obs}}$ and the BH mass at which $\Gamma(M_{\text{BH}})$ reaches maximum $M_{\text{BH,peak}}$, plotted against $M_{\text{BH,obs}}$, for each galaxy or cluster in our sample. The color indicates the difference in TDE rates calculated at $M_{\text{BH,peak}}$ and $M_{\text{BH,obs}}$. A linear fit is shown using the solid blue line. The dashed blue lines indicate where the y-axis is 0 (i.e., where $\Delta \log M_{\text{BH}}$ switches sign), which crosses the linear fit at $\log M_{\text{BH,obs}} \sim 6.7$ or $M_{\text{BH,obs}} \sim 5 \times 10^6 M_{\odot}$.

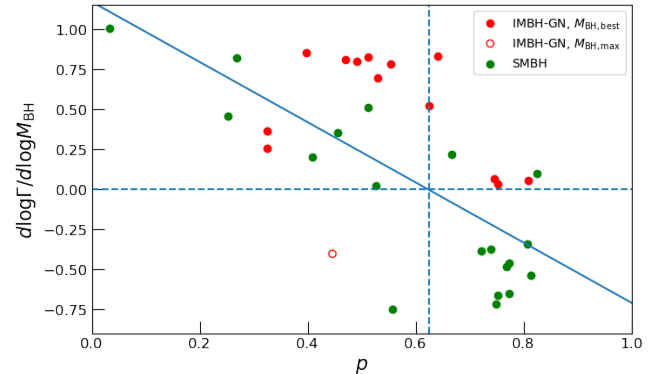


Figure 9. The gradient of $\Gamma(M_{\text{BH}})$ calculated at the observed $M_{\text{BH,obs}}$ plotted against the Sersic inner slope p (of the innermost stellar component) for each galaxy. The circle symbol style and color are consistent with Fig. 1 (a). The solid blue line shows the linear fit, and the dashed blue line marks where $d \log \Gamma / d \log M_{\text{BH}} = 0$. The curves cross at $p \sim 0.63$.

R_{eff} , which contributes to having $\Gamma(M_{\text{BH}})$ peak around the mass separation between the two populations.

4. CONCLUSION

In this work we compute the TDE rates and pinhole fractions for a sample of 23 observed IMBH TDE candidates which have realistic stellar profiles for their host galaxies and have BH masses constrained using dynamical measurements. Some of these IMBHs reside at the center of small galaxies (denoted as IMBH-GN), while others reside in globular clusters (denoted as IMBH-ON). We

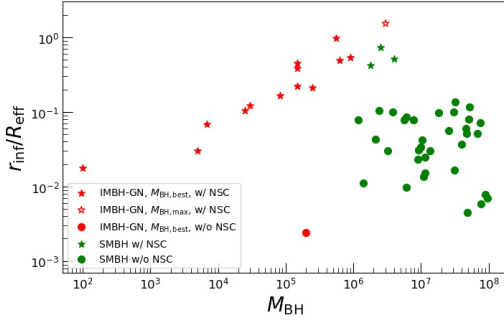


Figure 10. The ratio between the BH influence radius r_{inf} and the effective radius R_{eff} (of the innermost stellar component) of a galaxy plotted against M_{BH} for each galaxy. The symbol style and color are consistent with Fig. 1 (d).

compare the results of our TDE calculations for IMBHs with TDEs from SMBHs, and investigate how the TDE rate and pinhole fraction are affected by the stellar profile of the galaxy and the mass of the MBH. Furthermore, we also calculate the β -distributions and the volumetric rates of IMBH and SMBH TDEs. We summarize the key results below and present some additional technical details and derivations in the appendices:

- We find that the TDE rate for an IMBH hosting galaxy or cluster in our sample varies from $\sim 10^{-8}$ to $\sim 10^{-4} \text{ gal}^{-1}\text{yr}^{-1}$, which is comparable to the TDE rate for a SMBH hosting galaxy (Fig. 1). This implies that TDEs can serve as a promising probe for the detection of IMBHs, that remain a somewhat elusive population despite expectations of them being ubiquitous. Among the two IMBH populations, the TDE rate for an IMBH-GN is typically higher than that for an IMBH-ON.
- Contrary to the predictions from earlier works, we find that the TDE rate does not monotonically decrease when M_{BH} increases. The TDE rate from every galaxy generally increases as M_{BH} increases within the IMBH mass range of $10^{4-6} M_{\odot}$, while it decreases as M_{BH} moves into the SMBH regime for BH mass in excess of $10^6 M_{\odot}$ (as shown in Fig. 1 panel (b)). We have provided a fitting formula for the TDE rate per galaxy as a function of M_{BH} (Eqn. 18).
- IMBH TDEs mostly occur in the pinhole regime (Fig. 2). This implies that IMBH-TDEs, as compared to SMBH-TDEs, can more likely have deeply penetrating events (Fig. 6) and produce distinct observational signatures.
- The TDE rate for a galaxy is positively correlated to both its central stellar density ρ_0 and the inner

slope of the stellar density profile p (Fig. 4) when modeling the stellar component of the host galaxy with the Sersic model. Hence, we see that IMBHs embedded in a galaxy with a nuclear star cluster has a boosted TDE rate.

- The TDE pinhole fraction for a galaxy, on the other hand, depends mainly on the inner slope of the stellar profile p (Fig. 4). IMBH hosts tend to have low p (i.e., they have less concentrated stellar structures), which explains once again why IMBH-TDEs mostly occur in the pinhole regime.
- We compute the volumetric TDE rates as a function of M_{BH} around IMBHs and SMBHs (Eqn. 26), and the total volumetric TDE rates around both IMBHs and SMBHs and find them to be $\dot{N} \sim 10^{-7} \text{ Mpc}^{-3}\text{yr}^{-1}$. These theoretically estimated TDE rates are in general agreement with estimates derived from current observations.

We also note that the volumetric TDE rate obtained in this work depends sensitively on the assumed BHMF, which has a large degree of uncertainty in the IMBH mass range. Here we have adopted a BHMF obtained using observations of local AGNs for our calculations. However, the BHMF of dormant MBHs can be significantly different. In the future when a larger sample of IMBH TDEs is obtained, it will become possible to use the observed IMBH TDE rates to constrain the IMBH mass function conversely. A similar approach has been demonstrated by Yao et al. (2023) but mainly for SMBHs.

Last but not least, it is intriguing to ask why the number of the observed IMBH TDEs is lower than detected SMBH TDEs, if their intrinsic rates are in fact comparable. Up to now about a dozen observed TDEs are from MBHs with $M_{\text{BH}} < 10^6 M_{\odot}$ (Wevers et al. 2017, 2019). One possible reason for the discrepancy could be that dormant MBHs indeed have a BHMF different from the one used as mentioned above, which would suggest that the actual IMBH occupation fraction is quite low. Alternatively, it is also possible that IMBH TDEs may have characteristics different from classical predictions and current surveys tend to miss them. Moreover, TDEs from IMBHs come from small galaxies and stellar clusters, which are off the center in massive, bright galaxies. This adds difficulty in identifying the nature of these events. Besides, many automated pipelines for transient detection, including TDEs currently filter out off-center events, therefore preferentially missing IMBH TDEs. In fact, TDEs might serve to be an efficient way to detect off-center dormant IMBHs or the population that is accreting at very low rates (Ricarte et al.

2021a,b). However, such sources are also not expected to have an associated dense NSC (Natarajan in prep.). In general, a better understanding of the physics and environments of IMBH TDEs will be very useful for detecting this population of transients more effectively in the future and leveraging them to probe the elusive IMBH population.

We thank D. French, J. Greene, S. Li, M. Polkas, E. Ramirez-Ruiz, A. Seth, N. Stone, V. Tang, T. H. Wong and J. Woo for useful comments and discus-

sions. JC, LD, HF and RKC acknowledge the support from the National Natural Science Foundation of China (HKU12122309) and the Hong Kong Research Grants Council (HKU17314822, 27305119, 17304821). This research was supported in part by grant no. NSF PHY-2309135 to the Kavli Institute for Theoretical Physics (KITP). PN acknowledges support from the Gordon and Betty Moore Foundation and the John Templeton Foundation that fund the Black Hole Initiative (BHI) at Harvard University where she serves as one of the PIs.

REFERENCES

- Aleo, P. D., Malanchev, K., Sharief, S., et al. 2023, *ApJS*, 266, 9
- Angus, C. R., Baldassare, V. F., Mockler, B., et al. 2022, *Nature Astronomy*, 6, 1452
- Barth, A. J., Strigari, L. E., Bentz, M. C., Greene, J. E., & Ho, L. C. 2009, *ApJ*, 690, 1031
- Baumgardt, H. 2017, *MNRAS*, 464, 2174
- Binney, J. J. 2011, *Galactic Dynamics - 4*, IAC Talks, Astronomy and Astrophysics Seminars from the Instituto de Astrofísica de Canarias, id.331, ,
- Bond, J. R., Arnett, W. D., & Carr, B. J. 1984, *ApJ*, 280, 825
- Bromm, V., & Loeb, A. 2003, *ApJ*, 596, 34
- Cann, J. M., Satyapal, S., Abel, N. P., et al. 2019, *ApJL*, 870, L2
- Chen, J.-H., & Shen, R.-F. 2018, *ApJ*, 867, 20
- Cho, H., Woo, J.-H., Treu, T., et al. 2021, *ApJ*, 921, 98
- Dai, J. L., Lodato, G., & Cheng, R. 2021, *SSRv*, 217, 12
- Dai, L., McKinney, J. C., & Miller, M. C. 2015, *ApJL*, 812, L39
- Davis, B. L., Graham, A. W., & Cameron, E. 2019, *ApJ*, 873, 85
- Davis, T. A., Nguyen, D. D., Seth, A. C., et al. 2020, *MNRAS*, 496, 4061
- den Brok, M., Seth, A. C., Barth, A. J., et al. 2015, *ApJ*, 809, 101
- Di Matteo, T., Ni, Y., Chen, N., et al. 2023, *MNRAS*, 525, 1479
- Eracleous, M., Gezari, S., Sesana, A., et al. 2019, *Bulletin of the AAS*, 51, <https://baas.aas.org/pub/2020n3i010>
- Gallo, E., & Sesana, A. 2019, *ApJL*, 883, L18
- Gerssen, J., van der Marel, R. P., Gebhardt, K., et al. 2002, *AJ*, 124, 3270
- Gezari, S. 2021, *ARA&A*, 59, 21
- Greene, J. E., & Ho, L. C. 2006, *ApJL*, 641, L21
- Greene, J. E., Strader, J., & Ho, L. C. 2020, *ARA&A*, 58, 257
- Guillochon, J., & Ramirez-Ruiz, E. 2013, *ApJ*, 767, 25
- Jiang, Y.-F., Stone, J. M., & Davis, S. W. 2014, *ApJ*, 796, 106
- Kesden, M. 2012, *PhRvD*, 85, 024037
- King, I. R. 1966, *AJ*, 71, 64
- Kızıltan, B., Baumgardt, H., & Loeb, A. 2017, *Nature*, 542, 203
- Kochanek, C. S. 2016, *MNRAS*, 461, 371
- Kroupa, P. 2001, *MNRAS*, 322, 231
- Kuin, N. P. M., Wu, K., Oates, S., et al. 2019, *MNRAS*, 487, 2505
- Law-Smith, J., MacLeod, M., Guillochon, J., Macias, P., & Ramirez-Ruiz, E. 2017, *ApJ*, 841, 132
- Leloudas, G., Fraser, M., Stone, N. C., et al. 2016, *Nature Astronomy*, 1, 0002
- Lin, D., Strader, J., Carrasco, E. R., et al. 2018, *Nature Astronomy*, 2, 656
- Lodato, G., & Natarajan, P. 2006, *MNRAS*, 371, 1813
- Lützgendorf, N., Gebhardt, K., Baumgardt, H., et al. 2015, *A&A*, 581, A1
- Lützgendorf, N., Kissler-Patig, M., Gebhardt, K., et al. 2013, *A&A*, 552, A49
- MacLeod, M., Guillochon, J., Ramirez-Ruiz, E., Kasen, D., & Rosswog, S. 2016, *ApJ*, 819, 3
- Magorrian, J., & Tremaine, S. 1999, *MNRAS*, 309, 447
- Maksym, W. P., Ulmer, M. P., Eracleous, M. C., Guennou, L., & Ho, L. C. 2013, *MNRAS*, 435, 1904
- Margutti, R., Metzger, B. D., Chornock, R., et al. 2019, *ApJ*, 872, 18
- Martín-Navarro, I., & Mezcua, M. 2018, *ApJL*, 855, L20
- McKinney, J. C., Dai, L., & Avara, M. J. 2015, *MNRAS*, 454, L6
- Mockler, B., Guillochon, J., & Ramirez-Ruiz, E. 2019, *ApJ*, 872, 151

- Neumayer, N., Seth, A., & Böker, T. 2020a, *A&A Rv*, 28, 4
—, 2020b, *A&A Rv*, 28, 4
- Neumayer, N., & Walcher, C. J. 2012, *Advances in Astronomy*, 2012, 709038
- Nguyen, D. D., Seth, A. C., den Brok, M., et al. 2017, *ApJ*, 836, 237
- Nguyen, D. D., Seth, A. C., Neumayer, N., et al. 2019, *ApJ*, 872, 104
- Noyola, E., Gebhardt, K., Kissler-Patig, M., et al. 2010, *ApJL*, 719, L60
- Pechetti, R., Seth, A., Kamann, S., et al. 2022, *ApJ*, 924, 48
- Perera, B. B. P., Stappers, B. W., Lyne, A. G., et al. 2017, *MNRAS*, 468, 2114
- Perley, D. A., Mazzali, P. A., Yan, L., et al. 2019, *MNRAS*, 484, 1031
- Pfister, H., Dai, J. L., Volonteri, M., et al. 2021, *MNRAS*, 500, 3944
- Pfister, H., Toscani, M., Wong, T. H. T., et al. 2022, *MNRAS*, 510, 2025
- Pfister, H., Volonteri, M., Dai, J. L., & Colpi, M. 2020, *MNRAS*, 497, 2276
- Polkas, M., Bonoli, S., Bortolas, E., et al. 2023, *arXiv e-prints*, arXiv:2312.13242
- Portegies Zwart, S. F., Baumgardt, H., Hut, P., Makino, J., & McMillan, S. L. W. 2004, *Nature*, 428, 724
- Portegies Zwart, S. F., & McMillan, S. L. W. 2002, *ApJ*, 576, 899
- Prugniel, P., & Simien, F. 1997, *A&A*, 321, 111
- Ramirez-Ruiz, E., & Rosswog, S. 2009, *ApJL*, 697, L77
- Rees, M. J. 1988, *Nature*, 333, 523
- Ricarte, A., Tremmel, M., Natarajan, P., & Quinn, T. 2021a, *ApJL*, 916, L18
- Ricarte, A., Tremmel, M., Natarajan, P., Zimmer, C., & Quinn, T. 2021b, *MNRAS*, 503, 6098
- Rosswog, S., Ramirez-Ruiz, E., & Hix, W. R. 2009, *ApJ*, 695, 404
- Shiokawa, H., Krolik, J. H., Cheng, R. M., Piran, T., & Noble, S. C. 2015, *ApJ*, 804, 85
- Stone, N. C., & Metzger, B. D. 2016, *MNRAS*, 455, 859
- Stone, N. C., Vasiliev, E., Kesden, M., et al. 2020, *SSRv*, 216, 35
- Strubbe, L. E. 2011, PhD thesis, University of California, Berkeley
- Tang, V. L., Madau, P., Bortolas, E., et al. 2024, *ApJ*, 963, 146
- van Velzen, S. 2018, *VizieR Online Data Catalog*, J/ApJ/852/72
- van Velzen, S., & Farrar, G. R. 2014, *ApJ*, 792, 53
- Vasiliev, E. 2017, *ApJ*, 848, 10
- Wang, J., & Merritt, D. 2004, *ApJ*, 600, 149
- Wevers, T., van Velzen, S., Jonker, P. G., et al. 2017, *MNRAS*, 471, 1694
- Wevers, T., Stone, N. C., van Velzen, S., et al. 2019, *MNRAS*, 487, 4136
- Wong, T. H. T., Pfister, H., & Dai, L. 2022, *ApJL*, 927, L19
- Woo, J.-H., Cho, H., Gallo, E., et al. 2019, *Nature Astronomy*, 3, 755
- Yao, Y., Ravi, V., Gezari, S., et al. 2023, *ApJL*, 955, L6

APPENDIX

A. SAMPLES

We present here our sample of IMBH-GNs (Table. A.1), IMBH-ONs (Table. A.2), and SMBHs (Table.A.3).

Table A.1. IMBHs at Galaxies Nuclei

Name	n	$R_{\text{eff}} [pc]$	$\log_{10} \left(\frac{M_{\text{BH,best}}}{M_{\odot}} \right)$	$\log_{10} \left(\frac{M_{\text{BH,max}}}{M_{\odot}} \right)$	$\log_{10} \left(\frac{M_{\star}}{M_{\odot}} \right)$	f	$\log_{10} \Gamma$	reference
NGC5102 ₁	0.80	1.60	5.96		6.85	1.00	-3.99	1
NGC5102 ₂	3.10	32.00	5.96		7.76	0.93	-4.45	1
NGC5102 _b	3.00	1200.00	5.96		9.77	0.97	-5.66	1
NGC1493	2.36	2.60	5.40	5.90	6.30	0.94	-4.37	2
NGC3621	1.00	4.10		6.48	7.00	0.98	-4.51	3
NGC5206 ₁	0.80	3.40	5.80		6.23	1.00	-5.42	1
NGC5206 ₂	2.30	10.50	5.80		7.11	0.95	-4.57	1
NGC5206 _b	2.57	986.00	5.80		9.38	0.98	-6.45	1
NGC404 ₁	0.50	1.60	5.74		6.53	1.00	-4.63	4
NGC404 ₂	1.96	20.10	5.74		7.04	0.98	-5.63	4
NGC404 _b	2.43	640.00	5.74		8.93	0.99	-6.58	4
NGC4395 ₁	2.25	3.60	4.92		6.30	0.94	-4.73	6,7
NGC4395 _b	0.44	500.00	4.92		9.30	1.00	-9.50	6,7
NGC205 ₁	1.60	1.30	3.83		6.26	1.00	-4.92	1
NGC205 _b	1.40	516.00	3.83		8.99	1.00	-8.02	1
NGC1042	1.15	1.94	4.40	6.48	6.48	1.00	-5.27	2
NGC3423	1.20	4.18	5.18	5.85	6.48	1.00	-5.46	2
NGC428	1.05	3.36	4.48	4.85	6.48	1.00	-5.92	2
AT2020neh	3.20	1750.00	5.30		9.57	0.98	-6.33	7
NGC7793	1.27	7.70	3.70	5.90	6.90	1.00	-6.68	2
NGC2139	1.53	10.30	5.18	5.60	5.90	0.99	-6.73	2
NGC7424	0.91	7.40	5.18	5.60	6.00	1.00	-6.83	2
NGC300	1.10	2.90	2.00	5.00	6.00	1.00	-8.20	2

NOTE—Table of stellar profile parameters for IMBH-GNs. The parameters are (from left to right): the Sersic index n , the effective radius R_{eff} , best BH mass estimate $M_{\text{BH,best}}$, maximum BH mass estimate $M_{\text{BH,max}}$, mass of the stellar component M_{\star} , pinhole fraction f , and TDE rate Γ . The table is sorted by TDE rate from high to low. Some galaxies have nuclear star clusters (NSCs) and therefore are fitted with multi-component stellar profiles. These components are indicated by different lower indices, with numbers indicating the NSCs component and b indicating the bulge component. The stellar profiles and BH mass are obtained from the following literature: (1) Nguyen et al. (2019), (2) Neumayer & Walcher (2012), (3) Barth et al. (2009), (4) Davis et al. (2020), (5) den Brok et al. (2015), (6) Cho et al. (2021), (7) Angus et al. (2022). For the special case of NGC4395 which has mass measurements from two different methods (dynamical measurements giving $\log_{10}(M_{\text{BH}}/M_{\odot}) = 5.60$ (den Brok et al. 2015) and reverberation mapping giving $\log_{10}(M_{\text{BH}}/M_{\odot}) = 4.23$ (Woo et al. 2019; Cho et al. 2021)), we calculate the geometric mean of the two masses and use that to calculate the TDE rate and pinhole fraction.

B. SCALING OF THE DIFFUSION COEFFICIENT

In this section, we show in detail how the diffusion coefficient scales with the stellar mass distribution. We summarize the derivations in §8.3 in Binney (2011) and Appendix B in Pfister et al. (2022). The orbital averaged diffusion coefficient can be calculated by the following equation:

$$\bar{u}(E) = \frac{2}{P(E)} \int_{r_p}^{r_a} \frac{dr}{v_r} \lim_{R \rightarrow 0} \frac{\langle (\Delta R)^2 \rangle}{2R} \quad (\text{B1})$$

Table A.2. IMBHs Off Nuclei

Name	W_0	R_0	$\log_{10} \left(\frac{M_{\text{BH}}}{M_{\odot}} \right)$	$\log_{10} \left(\frac{M_{\star}}{M_{\odot}} \right)$	f	$\log_{10} \Gamma$	reference
NGC7078	10.82	0.20	3.39	6.71	1.00	-5.77	1
B023-G78	5.37	2.69	4.96	6.79	1.00	-5.90	2
NGC6388	11.00	0.41	4.45	6.08	1.00	-5.92	3
NGC6266	7.59	0.21	3.30	5.85	1.00	-5.96	4
NGC6624	10.82	0.13	3.88	4.86	1.00	-6.29	5
NGC6715	7.98	0.81	4.04	6.15	1.00	-6.42	6
OmegaCen	5.50	4.60	4.67	6.70	1.00	-6.89	7
NGC104	12.00	0.42	3.36	5.89	1.00	-7.35	8

NOTE—Table of stellar profile parameters for IMBH-ONs. The parameters are (from left to right): the dimensionless potential W_0 , the King radius R_0 , BH mass estimate M_{BH} , stellar mass M_{\star} , pinhole fraction f , and TDE rate Γ . The table is sorted by TDE rate. The stellar profiles and BH mass are obtain from the following literature: (1) Gerssen et al. (2002), (2) Pechetti et al. (2022), (3) Lützgendorf et al. (2015), (4) Lützgendorf et al. (2013), (5) Perera et al. (2017), (6) Baumgardt (2017), (7) Noyola et al. (2010), (8) Kızıltan et al. (2017).

where $P(E)$ is the orbital period, v_r is the radial velocity of the orbit, and r_a and r_p are the apocentre and pericentre radius respectively. The last term is the local diffusion coefficient defined as:

$$\lim_{R \rightarrow 0} \frac{\langle (\Delta R)^2 \rangle}{2R} = \frac{32\pi^2 r^2 G^2 m_{\text{scatt}}^2 \ln \Lambda}{3J_c(E)^2} \left(3I_{1/2}(E) - I_{3/2}(E) + 2I_0(E) \right) \quad (\text{B2})$$

which can be represented in terms of the moments of the stellar distribution function (DF) $f(E)$ (Eqn. 6):

$$I_0(E) = \int_0^E f(E') dE \quad (\text{B3})$$

$$I_{n/2}(E) = [2(\Psi - E)]^{-n/2} \int_E^{\Psi} [2(\Psi - E')]^{n/2} f(E') dE \quad (\text{B4})$$

We note that the diffusion coefficient is independent on the mass of the disrupted star, but instead depends on the mass of the background stars m_{scatt} . Therefore, when considering a distribution of stellar mass with in IMF $\phi(m)$, we take $m_{\text{scatt}}^2 = \langle m^2 \rangle = \int m^2 \phi(m) dm$. However, $f(E)$ itself is dependent on the stellar mass. Hence, we also need to scale it with $1/\langle m \rangle$. This means that the DF moments should also scale with $1/\langle m \rangle$. Combining these factors, we have the averaged orbital diffusion coefficient for a stellar population with distribution of stellar masses as:

$$\bar{u}(E) = \frac{\langle m^2 \rangle}{\langle m \rangle} \bar{u}_{\text{mono}}(E) \quad (\text{B5})$$

C. EFFECTS OF M_{BH} ON THE TDE PINHOLE FRACTION

In this section, we demonstrates how M_{BH} affects the TDE pinhole fraction f using the example of an IMBH host galaxy NGC1042. NGC1042 has $M_{\text{BH,best}} = 2 \times 10^4 M_{\odot}$ and $M_{\text{BH,max}} = 3 \times 10^6 M_{\odot}$.

We plot the differential TDE rate $d^2\Gamma/dEd \ln \beta$ and the cumulative TDE rate fraction $\Gamma(E)/\Gamma_{\text{total}}$ in Fig. C.1 of NGC1042 for both $M_{\text{BH,best}}$ and $M_{\text{BH,max}}$. One can see from the upper panels that for the lower BH mass $M_{\text{BH,best}}$, most TDEs happen in the pinhole regime (to the left of the dashed line corresponding to $q = 1$) as opposed to the diffusive regime (to the right of the dashed line). This is simply because a lower M_{BH} allows a higher maximum β at which the star can still be disrupted before plunging into the BH event horizon, as demonstrated by the lower panels. This higher cut-off value of β increases the contribution of the pinhole regime, since the pinhole regime allows β from large values, whereas the diffusive regime have $\beta \sim 1$.

Table A.3. SMBHs

Name	n	$R_{\text{eff}} [pc]$	$\log_{10} \left(\frac{M_{\text{BH}}}{M_{\odot}} \right)$	$\log_{10} \left(\frac{M_{\star}}{M_{\odot}} \right)$	f	$\log_{10} \Gamma$
Circinus ₁	1.09	8.00	6.25	7.57	0.99	-4.53
Circinus _b	2.21	680.00	6.25	10.12	0.98	-5.30
ESO558 – G009	1.28	330.00	7.26	9.89	0.98	-5.56
IC2560	2.27	4210.00	6.49	9.63	0.98	-7.48
J0437 + 2456	1.73	420.00	6.51	9.90	0.98	-5.43
M32 ₁	2.70	4.40	6.40	7.16	0.78	-3.80
M32 ₂	1.00	516.00	6.40	8.29	1.00	-8.12
M32 _b	1.60	108.00	6.40	8.90	0.98	-5.26
MilkyWay ₁	2.00	6.00	6.60	7.64	0.87	-3.72
MilkyWay _b	1.30	1040.00	6.60	9.96	0.99	-6.73
Mrk1029	1.15	300.00	6.33	9.90	1.00	-5.89
NGC0253	2.53	930.00	7.00	9.76	0.95	-5.59
NGC1068	0.71	510.00	6.75	10.27	1.00	-6.68
NGC1300	4.20	1720.00	7.71	9.42	0.69	-6.42
NGC1320	3.08	610.00	6.78	10.25	0.92	-4.30
NGC1426	4.95	4150.00	7.69	10.98	0.55	-4.91
NGC2273	2.24	460.00	6.97	9.98	0.95	-4.92
NGC2634	4.54	2930.00	7.95	11.00	0.36	-5.37
NGC2960	2.59	810.00	7.06	10.44	0.93	-4.73
NGC3031	2.81	610.00	7.83	10.16	0.64	-5.52
NGC3079	0.52	470.00	6.38	9.92	1.00	-7.89
NGC3227	2.60	1830.00	7.88	10.04	0.83	-6.75
NGC3368	1.19	310.00	6.89	9.81	0.99	-5.68
NGC3393	1.14	430.00	7.49	10.23	0.97	-5.77
NGC3627	3.17	570.00	6.95	9.74	0.91	-4.77
NGC4151	2.24	570.00	7.68	10.27	0.82	-5.36
NGC4258	3.21	1540.00	7.60	10.05	0.82	-5.78
NGC4303	1.02	140.00	6.58	9.42	1.00	-5.60
NGC4388	0.89	1870.00	6.90	10.07	1.00	-7.71
NGC4458	10.10	4090.00	6.76	10.27	0.48	-2.88
NGC4478	3.11	1130.00	7.50	10.56	0.80	-4.91
NGC4501	2.33	1150.00	7.13	10.11	0.95	-5.58
NGC4736	0.93	210.00	6.78	9.89	1.00	-5.64
NGC4826	0.73	370.00	6.07	9.55	1.00	-7.41
NGC4945	3.40	470.00	6.15	9.39	0.95	-4.83
NGC5017	5.11	1910.00	7.98	10.93	0.19	-4.96
NGC5495	2.60	1760.00	7.04	10.54	0.95	-5.31
NGC5765	1.46	720.00	7.72	10.04	0.95	-6.34
NGC5831	4.72	3360.00	7.89	11.08	0.39	-5.15
NGC6264	1.04	840.00	7.51	10.01	0.99	-6.70
NGC6323	2.09	830.00	7.02	9.86	0.97	-5.70
NGC7582	2.20	510.00	7.67	10.15	0.83	-5.39
UGC3789	2.37	380.00	7.06	10.18	0.92	-4.48
UGC6093	1.55	1360.00	7.41	10.35	0.97	-6.26

NOTE—Table of stellar profile parameters for SMBHs obtained from Pfister et al. (2020). The parameters are (from left to right): the Sersic index n , effective radius R_{eff} in pc, BH mass M_{BH} , stellar mass M_{\star} , pinhole fraction f , and TDE rate Γ . Some galaxies are fitted with multiple components (NSCs or bulge), which are indicated by different lower indices (1,2 or b respectively).

NGC1042

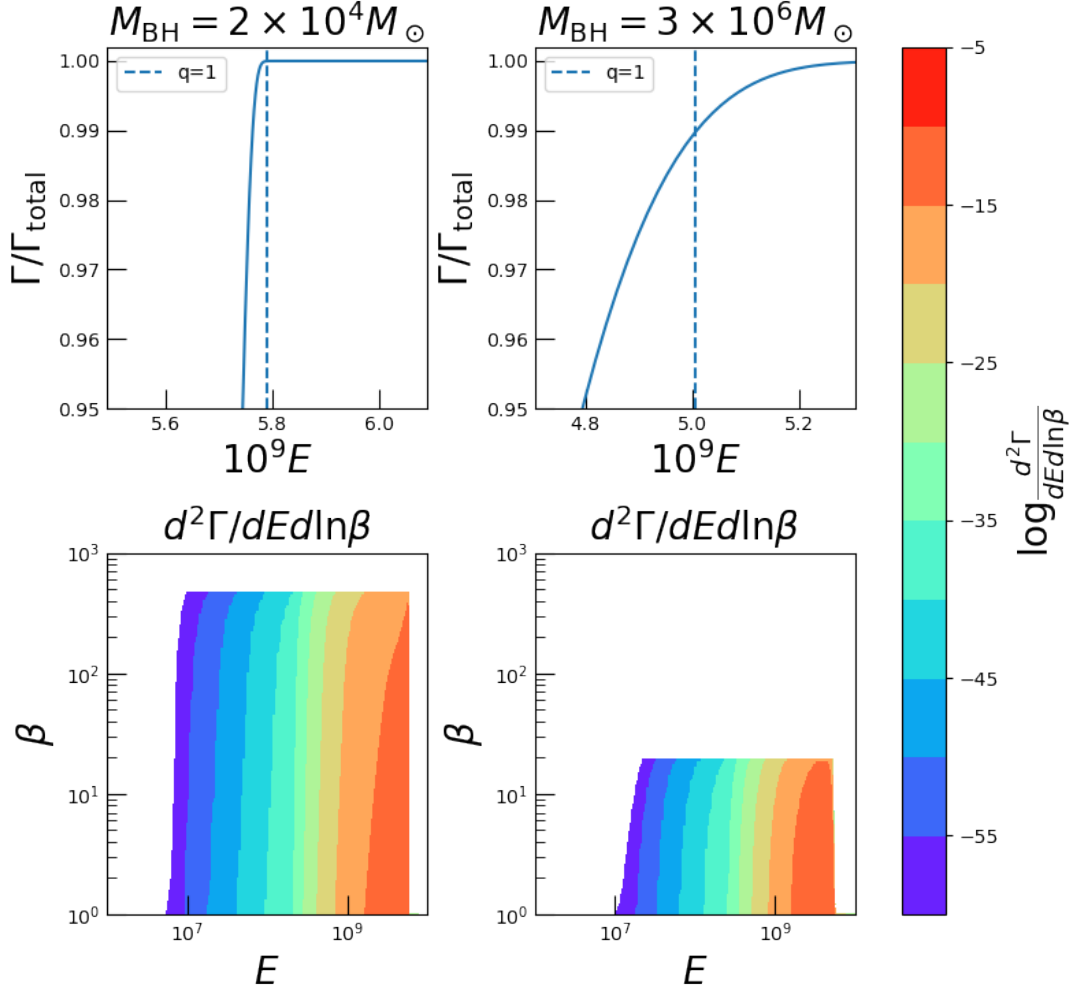


Figure C.1. The TDE rate of an IMBH host galaxy NGC1042 calculated using $M_{\text{BH,best}}$ (left) and $M_{\text{BH,max}}$ (right). The upper row shows the cumulative TDE rate fraction as a function of E . The blue vertical dashed line indicates $q = 1$, which is the boundary separating the pinhole regime (left side) and diffusive regime (right side). The lower row are contour plots showing how the differential TDE rate $d^2\Gamma/dEd\ln\beta$ depends on β (penetration parameter) and E (orbital specific energy).

At the same time, one can also see that the boundary between the pinhole regime and the diffusive regime shifts to a higher E for the lower M_{BH} . This is because M_{BH} is related to the size of the loss cone R_{lc} (Eqn. 11). When M_{BH} decreases, R_{lc} also decreases, which in turn increases the E at which the $q = 1$ boundary lies (Eqn. 12). This also contributes to the higher pinhole fraction for the lower M_{BH} .